Modelling the Time-Variability of the Ionospheric Electric Potential (TiVIE)

M.-T. Walach[1], A. Grocott[1]

[1] Physics Department, Lancaster University, Lancaster, LA1 4YB, UK

Key Points:

- We propose a new statistical model of the ionospheric electric potential.
- The model is derived from line-of-sight plasma flow measurements.
- The model captures the time dependence of solar wind forcing, substorms and geomagnetic storms.

Corresponding author: Maria-Theresia Walach, `m.walach@lancaster.ac.uk`

Abstract

We present a statistical model of the ionospheric electric potential derived from line-of-sight plasma velocity measurements from the Super Dual Auroral Radar Network (SuperDARN). Electric potential patterns are produced using an established technique that models the ionospheric electric potential as a spherical harmonic expansion. Improvements over existing models are achieved by the use of novel parameterizations that capture three major sources of time-variability of the coupled solar wind-magnetosphere-ionosphere system. The first source of variability relates directly to the time-dependence of the system on the upstream solar wind conditions, specifically the strength and orientation of the interplanetary magnetic field. The magnetosphere-ionosphere system is not static under continuous driving by the solar wind but evolves with time, even if the solar wind conditions themselves remain steady. We account for this by defining a solar wind steadiness timescale with which we parameterize the electric potential. The second source of variability relates to the storage and release of energy in the magnetosphere that is associated with magnetospheric substorms. The electric potential evolves throughout the substorm cycle, and its morphology is strongly influenced by the location of substorm onset. We therefore parameterize by substorm onset location and the time relative to substorm onset. Lastly we account for the variability introduced by geomagnetic storms. The ionospheric electric potential evolves differently through each phase of a storm, so we parameterize by storm phase. We discuss the details of the model, and assess its performance by comparison to other models and to observations.

Plain Language Summary

The ionosphere, one of the upper layers of the atmosphere, contains plasma that moves, generating electric fields and currents. These electric fields and currents are vital for generating space weather effects on Earth, directly influencing the magnetosphere-ionosphere system, such as aurora location and plasma flows. Plasma flows are governed by the system's time history and external drivers like the solar wind. Due to their complexity, these flows are hard to model, and most space weather models lack time-history information.

We present a statistical model of the ionospheric electric potential, derived from radar data. Our model improves on existing ones by capturing three major sources of time-variability and history of the magnetosphere-ionosphere system: interplanetary magnetic field strength, orientation and timescale of solar wind steadiness; and energy release during magnetospheric substorms; and progression through geomagnetic storms. We assess the model's performance through comparisons with other models and observations. The electric potential is directly related to the electric fields and plasma flows and this model is therefore of general relevance to space weather.

1 Introduction

Ionospheric electric fields, driven by solar wind-magnetosphere-ionosphere coupling, play an important role in the dynamics of the upper atmosphere, transferring heat and momentum to the neutral atmosphere via ion drag and Joule heating (e.g. Huang et al., 2012). This is an important aspect of space weather that is incorporated into atmospheric models, although presently quite outdated empirical plasma convection patterns are used to specify the electric field or electric potential (as discussed by Liu et al., 2018; Orr et al., 2023). The morphology of the ionospheric electric potential has traditionally been described in terms of the upstream solar wind driver; the speed of the solar wind and the strength and orientation of the interplanetary magnetic field (IMF). The orientation of the IMF is often quantified by the clock angle, θ, the angle the field vector makes with the Geocentric Solar Magnetospheric (GSM) north direction. To a first approximation the electric potential can be well ordered by a characterisation which involves the speed, IMF strength and θ and various empirical models of the ionospheric electric potential have been produced this way (e.g. Ruohoniemi & Greenwald, 2005; Pettigrew et al., 2010; Thomas & Shepherd, 2018). A limitation of these models is that they provide outputs that are the same regardless of how the time history of the magnetosphere or solar wind has evolved, whereas the dynamics of the coupled magnetosphere-ionosphere system are known to vary on a variety of timescales from minutes to hours. This is particularly problematic on the night side of the planet where convection is driven by dayside reconnection but also magnetotail reconnection that proceeds somewhat independently of the conditions in the solar wind (Cowley & Lockwood, 1992). The objective of the Time-Variable Ionospheric Electric potential (TiVIE) model is to better represent the ionospheric electric potential by using novel parameterizations that capture the major sources of time-variability of the coupled solar wind-magnetosphere-ionosphere system.

The first source of variability relates directly to the dependence of the system on the time-variability of the upstream solar wind conditions, specifically the strength and direction of the IMF. The magnetosphere-ionosphere system is not static under continuous driving by the solar wind but evolves with time, even if the solar wind conditions themselves remain steady. For example, so-called Tail Reconnection during IMF-Northward Non-substorm Intervals (TRINNIs) have been found that produce a distinct signature in the nightside ionospheric electric potential pattern (e.g. Milan et al., 2005; Grocott et al., 2007, 2008). TRINNI patterns have been reported in a number of case studies in which they were observed after the IMF had been steadily northward, but B_Y-dominated, for at least 4 hours (e.g. Grocott et al., 2003, 2004, 2005). This time-dependence was further addressed by Grocott and Milan (2014) who considered different timescales over which a given IMF state had been uninterruptedly maintained. They found the ionospheric electric potentials to be strongly dependent on this IMF 'steadiness' timescale, with the longer timescales tested (5 to 10 h) resulting in electric potential patterns that differed considerably from models that do not consider different steadiness timescales.

The second source of variability relates to the storage and release of energy in the magnetosphere that is associated with substorms. The electric potential evolves throughout the substorm cycle according to substorm phase (e.g. Morelli et al., 1995; Lewis et al., 1997; Yeoman et al., 2000; Grocott et al., 2002; Provan et al., 2004; Grocott et al., 2006). Rather than being controlled by the concurrent solar wind conditions, the electric potential morphologies during substorms are therefore more directly linked to the dynamics of the magnetotail. Limited attempts to account for this in electric potential models have been made, for example, Weimer (2001) included a substorm parameterization based on the AL auroral electrojet index. This fails to take into account the location of the substorm onset in the tail, however. Whilst onset is typically observed in the near-Earth pre-midnight sector tail (Nagai et al., 1998), the location can vary significantly and may map to a range of latitudes and local times in the ionosphere (Frey et al., 2004). The electric potential morphology has been found to be highly dependent on both substorm onset latitude (Grocott et al., 2009) and local time (Grocott et al., 2010, 2017). This local time dependence, in particular, is found to override any pre-existing IMF B_y-induced asymmetry in the midnight-sector electric potential pattern (Grocott et al., 2017). This makes substorm onset location a critical parameter in describing the patterns that cannot be accounted for with solar wind parameterizations alone.

A third source of variability is introduced by geomagnetic storms, with the ionospheric electric potential evolving differently through each storm phase (e.g. Walach & Grocott, 2019; Walach et al., 2021). (Gillies et al., 2011) found that the electric potential becomes enhanced during the main phase of the storm, with the degree of enhancement being related to the strength of the storm. They also found that the electric potential enhancement occurred in concert with an increase in IMF B_z. This might imply that the conditions in the solar wind would be sufficient to parameterize the electric potential. Closer inspection, however, reveals changes that cannot be directly attributed to the solar wind. Walach et al. (2021) found evidence of a rotation of the convection throat from a slight alignment with the late morning sector to be more sun-aligned. This rotation evolves throughout the main phase, but it is not accompanied by a corresponding rotation in the IMF. Walach et al. (2021) further found an enhancement of the dayside electric potentials, as the main phase of a geomagnetic storm evolves. This result is consistent with the findings from Coxon et al. (2023) who found that the dayside field aligned electric currents also enhance during geomagnetic storms. Walach and Grocott (2019) further considered the difference between the electric potentials driven during geomagnetically active times and those characterised solely by the level of solar wind driving. They found quite similar peak electric potential magnitudes for both categories, but very different spatial extents. During active times (Sym-H < -80 nT) the convection generally extends to lower latitudes ($45°$ to $55°$) with the most likely occurrence at $\sim 52°$ whereas during non-storm times (but times when the magnetosphere was still being strongly driven, as determined by an IMF strength of $> 8\,\mathrm{nT}$ and the clock angle magnitude, $|\theta| > 100°$) the distribution of convection coverage stretches over a broader and higher latitude range ($50°$ to $70°$) with a most commonly observed value at $\sim 65°$ in AACGM v2 coordinates (Shepherd, 2014).

These three sources of variability: solar wind driving, storage and release (substorms) and geomagnetic storms, all contribute to the time-dependent evolution of the ionospheric electric potential, yet remain unresolved in most current electric potential models. To improve our upper-atmospheric modelling capabilities, a more realistic ionospheric electric potential model is therefore desirable. We have developed such a model, the 'Time-Variable Ionospheric Electric potential' model, hereafter referred to as 'TiVIE'. TiVIE is pronounced as /tivi/, which rhymes with TV, the abbreviation for television, and is based on recent results using observations from the Super Dual Auroral Radar Network (SuperDARN). In this paper we describe the model and the methods used in its derivation. We also present the results of a simple validation exercise in which we compare the model outputs to observations.

2 Data Sets and Methodology

In this section we provide brief details of the data sets and methodology employed in deriving the TiVIE model.

2.1 SuperDARN

Large-scale observations of the ionospheric electric potential have been provided by the Super Dual Auroral Radar Network (SuperDARN) from 1995 to the present. SuperDARN is an ever-evolving international array of HF ionospheric radars located in the polar regions of both hemispheres whose fields-of-view cover much of the polar, auroral and subauroral regions. Although SuperDARN is located in both northern and southern hemispheres, TiVIE is based only on data from the northern network owing to the wider radar coverage necessary for TiVIE to capture the mid-latitudes. We briefly outline the SuperDARN data processing here and how we produce the SuperDARN data archive, which was used to build TiVIE. The SuperDARN Map Potential archive that we use is produced in the same way as D4 in Walach, Grocott, Staples, and Thomas (2022), so we refer the interested reader to this paper.

Figure 1 shows the fields-of-view of the SuperDARN radars in the northern hemisphere in AACGM-v2 coordinates (Shepherd, 2014). The colours indicate the different latitude bands that the radars are located in: polar (green), auroral (blue) and mid-latitude (red). Each radar measures the line-of-sight (LOS) Doppler velocity, $\mathbf{v_0}$, of ionospheric plasma irregularities from which the radars scatter (Greenwald et al., 1995; Chisham et al., 2007). During the common modes used for convection maps, the radars scan through 16 beams (look directions) making observations at 75 or more locations along each beam

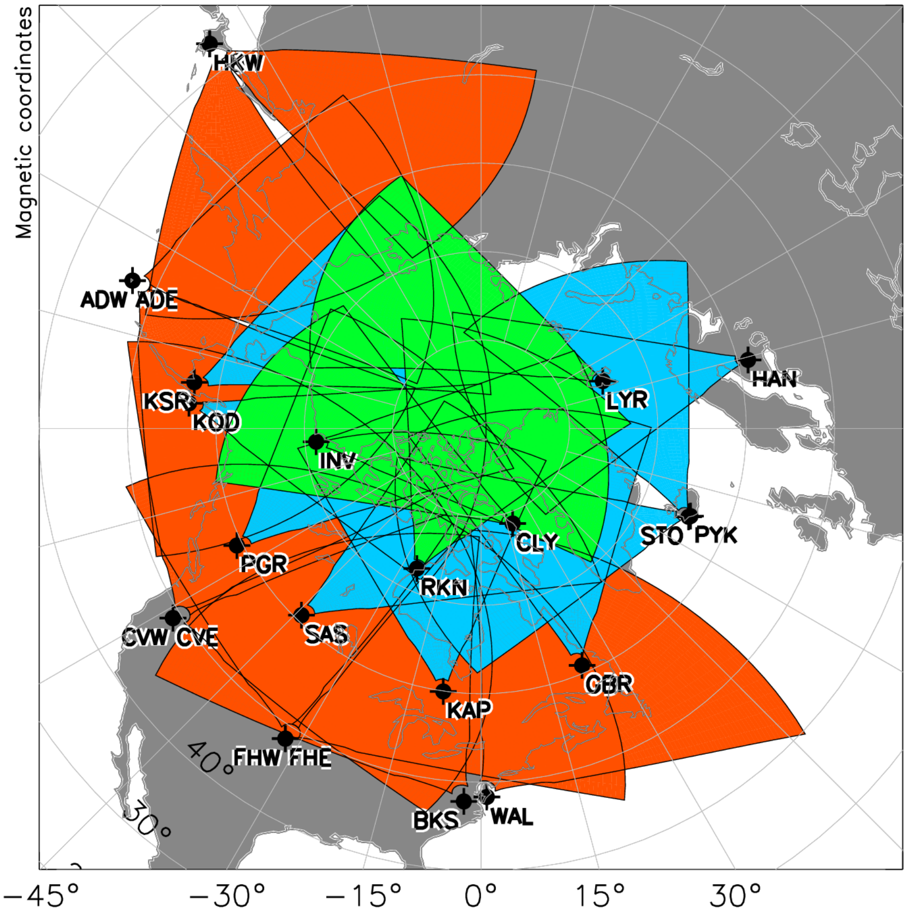

Figure 1. Fields of view of the northern hemisphere SuperDARN array as of August 2020. The radars are located in three latitude bands, nominally defined as: polar (green), auroral (blue) and subauroral (red). The plot was made by Virginia Tech (https://vt.superdarn.org).

at between 180 km and over 3500 km in range. The LOS velocities are derived from linear fits to the phase of the autocorrelation function of the backscattered radar signals. At the time of writing, and in the results presented here, this fitting is performed using the FITACF2.5 library contained in version 4.2 of the Radar Software Toolkit, RST (SuperDARN Data Analysis Working Group et al., 2018). The fitted velocities equivalently provide a measure of the convection electric field, $\mathbf{E}$, (given by $\mathbf{E} = -(\mathbf{v} \times \mathbf{B})$, where $\mathbf{B}$ is the ionospheric magnetic field vector and $\mathbf{v}$ is the plasma drift vector). The electrostatic potential Φ is defined by $\mathbf{E} = -\nabla\Phi$ (Ruohoniemi & Baker, 1998). Due to the mathematical definition of the gradient, the electric field has a higher dependence on the coordinate system (e.g. altitude and directionality), whereas the electric potential is a scalar and thus easier to use. Typically SuperDARN observes the F-region ionosphere at > 250 km, nevertheless, previous studies of Joule heating have demonstrated the validity of assuming height-independent $\mathbf{B}$ and $\mathbf{E}$ vector fields down to peak heating altitudes of ~ 160 km (e.g. Baker et al., 2004). SuperDARN observations thus provide an extremely useful tool not only for studying solar wind-magnetosphere-ionosphere coupling, but ionosphere-thermosphere coupling as well.

To produce each distinct convection map pattern, the sorted LOS vectors are mapped onto an equal-area magnetic latitude (MLAT) - magnetic local time (MLT) grid in Altitude-

Adjusted Corrected Geomagnetic Coordinates (AACGM v2)(Baker & Wing, 1989; Shepherd, 2014) in 2-min temporal bins using the "gridding" technique (Ruohoniemi & Baker, 1998) that is also contained within the RST toolkit. In performing the gridding of the LOS data we use only the "Common Time" radar data, in which the radars were run in a standard operating mode using 45-km range separation and 1 or 2 min total scan integrations times. We also apply the "range limit" criteria in which only observations from slant ranges greater than 800 km and less than 2000 km are included (after Thomas and Shepherd (2018)). This limits contamination by lower-velocity E region echoes at near ranges (Chisham & Pinnock, 2002) and minimises geolocation inaccuracies that become more significant at further ranges (Chisham et al., 2008).

To produce the large-scale convection patterns, the maps of gridded velocity vectors are combined. An established technique for combining the LOS measurements involves fitting them to a sixth order expansion of the ionospheric electric potential in spherical harmonics (Ruohoniemi & Baker, 1998), which is readily performed with RST (SuperDARN Data Analysis Working Group et al., 2018). In the spherical harmonic analysis, the modelled electric fields, $\mathbf{E_m}$, are converted to equivalent velocity vectors, $\mathbf{v_m}$, according to $\mathbf{v_m} = (\mathbf{E_m} \times \mathbf{B})/B^2$. The global sum of the differences between the observed velocity magnitudes and the parallel component of the modelled velocities are minimised, where the observed velocity magnitudes are v_0 (i.e. $v_0 = |\mathbf{v_0}|$) and the parallel component of the modelled velocity vectors is $(\mathbf{v_m} \cdot \mathbf{v_0})/v_0$. The value of the magnetic field, $\mathbf{B}$, used in the above calculation is determined from the IGRF-12 model, which we specify using the AACGM-v2 library in RST (Shepherd, 2014). To appropriately scale the patterns, a zero potential boundary at the equatorward edge of the convection pattern is required (Ruohoniemi & Baker, 1998). This is determined by fitting the Heppner-Maynard boundary (HMB) to the data (Shepherd & Ruohoniemi, 2000; Heppner & Maynard, 1987), which is circular on the nightside but lies at higher latitudes on the dayside. The usual procedure is for the HMB to be set according to an automated assessment of the available observations. This is not always reliable, but works well for individual SuperDARN maps when the number of backscatter echoes per map, n, is high ($n \geq 200$ (Walach, Grocott, Staples, & Thomas, 2022)). For our SuperDARN convection maps, we utilise the method from Imber et al. (2013) and Walach, Grocott, Staples, and Thomas (2022), which uses the latitude where three radar velocity measurements are greater than 100 m/s to define the HMB. Usually when high-resolution (1 to 2 minute) convection maps are produced using this method, the often sparsely distributed data are supplemented with data from an empirical model (e.g. Ruohoniemi & Greenwald, 1996; Cousins & Shepherd, 2010; Thomas & Shepherd, 2018). This empirical model is often referred to as "the background model" and we use the most recent one from Thomas and Shepherd (2018) for our dataset and a time-resolution of 2 minutes. In summary, our SuperDARN dataset is processed using standard SuperDARN techniques. Walach, Grocott, Staples, and Thomas (2022) and Walach, Grocott, Thomas, and Staples (2022) provide statistical analyses of the dataset (equivalent to D4 in their papers) in comparison to other processing methods and historical versions of the convection maps.

2.2 Parameterizing the TiVIE model

Previous models constructed with SuperDARN data do not account for the variability in the time-dependence of the magnetospheric response to the solar wind driver. In developing TiVIE we have isolated three sources of time-variability which we incorporate into three different TiVIE modes in order to better capture the time-dependence.

The flowchart in Figure 2 shows the different steps involved in producing the TiVIE model and the outputs shown later, as well as the processing differences in the TiVIE modes. In this section, we explain how TiVIE is parameterized and how we utilise the SuperDARN data archive to produce TiVIE. In step 1 in Fig. 2, an archive of fitted 2-

minute SuperDARN convection maps is first made using the method described in section 2.1. TiVIE can produce 3 different modes.

In step 2 in Fig. 2, the time interval and TiVIE mode is selected. Mode 1 is the IMF mode, mode 2 is the substorm mode and mode 3 is the geomagnetic storms mode. In Fig. 2 the mode-specific steps are outlined by the coloured boxes, which relate to modes 1 (yellow), 2 (green) and 3 (pink), whereas common steps are outlined by grey boxes. A large proportion of the TiVIE processing is inspired by the data combination processes employed by the Thomas and Shepherd (2018) SuperDARN model, which established the current best-practice for producing statistical convection patterns and is outlined in the steps 3 to 7 below. For constructing both modes 1 and 3, we utilize SuperDARN data from the years 2012-2018, the same as in Walach, Grocott, Staples, and Thomas (2022); Walach, Grocott, Thomas, and Staples (2022), whereas mode 2 uses data from 2000-2005, the same as in Grocott et al. (2017), which covers the Frey list. These time periods were used for consistency with Walach, Grocott, Staples, and Thomas (2022); Walach, Grocott, Thomas, and Staples (2022); Grocott et al. (2017) but in principle, this could be extended to other years. All radars available for these time periods in the northern hemisphere were used.

In step 3 in Fig. 2, the time periods are filtered based on the IMF or geomagnetic conditions of the chosen mode. We now explain the binning of each mode separately: Mode 1 employs a similar method to that discussed in detail by Grocott and Milan (2014). Using solar wind data from the OMNI database we sort the gridded radar data into bins of different solar wind conditions, much like previous models have done. For mode 1 we use bins similar to those employed by Ruohoniemi and Greenwald (2005), i.e. parameterized by IMF strength and clock angle. TiVIE uses IMF magnitude bins of $0-3\,\mathrm{nT}$, $3-5\,\mathrm{nT}$, $5-10\,\mathrm{nT}$ and $\geq 10\,\mathrm{nT}$; and 16 clock angle bins of 50° width. The clock angle bin centres are separated by 22.5° such that there is overlap between three consecutive clock angle bins (i.e. the clock angle bins are centred on 180°, -157.5°, -135°, -112.5°, -90°, -67.5°, -45°, -22.5°, 0°, 22.5°, 45°, 67.5°, 90°, 112.5°, 135°, 157.5°). These clock angle bins and IMF strength bins were chosen to optimise data availability whilst maintaining flexibility to represent different IMF directions. If a measurement falls into more than one bin, it is counted for each bin where the criterion is met. This allows the model to be smooth across bins without the need for explicit smoothing. In addition, however, we also sort according to how long those conditions had been steadily met. This means that the conditions have to be met 90% of the time. The latter criterion we define as the 'solar wind steadiness timescale', τ_B. The values used for τ_B will typically range between 20 mins and 10 hours, although the bin sizes tend to increase as τ_B increases, owing to the reduced number of intervals with high τ_B. Figure 1 of Grocott and Milan (2014) presents the data distribution with respect to the clock angle and τ_B bins. Grocott and Milan (2014) showed that for all bins only two (southward IMF and longest τ_B) had low occurrence numbers. For TiVIE we use τ_B of $20-30$ minutes, $30-40$ minutes, $40-60$ minutes, $60-90$ minutes, $90-120$ minutes, $120-240$ minutes, $240-360$ minutes and longer than 360 minutes. With mode 1, TiVIE is thus able to provide different convection patterns, for the same instantaneous solar wind conditions, but in the very different cases that the solar wind conditions have, for example, either changed very recently, or have been stable for a longer time.

Mode 2 is the substorm mode. This mode employs a similar method to that discussed by Grocott et al. (2017) and produces a superposed epoch analysis with respect to substorm onset. Here, observations of substorm onsets, from a published list are used to sort the radar data into bins of substorm onset location (i.e. within a specified magnetic latitude and MLT range) and substorm epoch time (i.e. the time relative to substorm onset). We utilize the list from Frey et al. (2004), but other lists such as Forsyth et al. (2015), Newell and Gjerloev (2011), or Ohtani and Gjerloev (2020) are available. Onsets tend to occur over a latitude range of 55° to 75° and MLT range of 20 to 03 hours, with a peak occurrence close to 66° and 23 MLT. Around this peak the size of the bins may be small, with the bin size necessarily becoming larger towards the extremes of these ranges in order to maintain sufficient events (see, e.g., Figure 3(a) of Grocott et al. (2010)). Given that we are interested in the time-evolution of the pattern, we only include isolated substorms (i.e. those occurring at least 2 hours after a previous onset). This avoids the situation where effects of multiple substorms overlap. In the Frey et al. (2004) list, for example, there are 1979 northern hemisphere substorm onsets with which to parameterize TiVIE. Mode 2 enables TiVIE to more accurately represent the nightside ionospheric convection pattern in comparison to models parameterized by solar wind conditions.

Mode 3 is the geomagnetic storm mode. This mode employs a superposed epoch analysis with respect to storm phase, similar to that discussed by Walach and Grocott (2019); Walach et al. (2021). In this case, the convection pattern has been parameterized by the time relative to the start and end of each storm phase which is identified using the Sym-H index according to the method described by Walach and Grocott (2019). In brief, this is accomplished as follows: First, the minimum in Sym-H is found, which must be $< -80\,\mathrm{nT}$ for a storm to be identified. The time of this minimum marks the beginning of the recovery phase with the end of the recovery phase being identified where Sym-H next reached a quiet level ($-15\,\mathrm{nT}$). The beginning of the main phase is defined as the last point where Sym-H crossed the quiet level. The initial phase is then characterised by the maximum in Sym-H, above the quiet level, prior to the main phase. The beginning of the initial phase is where Sym-H last surpassed the quiet level prior to this. Since the development of the mid-latitude "StormDARN" extension to SuperDARN (i.e. from 2012-2018) there were 52 storms identified by the Walach and Grocott (2019) method that are available for TiVIE parameterization. Sorting the radar data in this way enables TiVIE to distinguish differences in the convection patterns that arise under conditions of strong solar wind driving that evolve throughout the storm.

The nature of the interval sorting is tailored according to the different TiVIE modes as described above, but the process for combining those data is common. After having identified and filtered the relevant time periods for each mode in step 3, we combine the gridded LOS data from the SuperDARN archive of Map Potential convection maps in step 4, Fig. 2: We combine the data onto a common quasi-magnetic local time grid. This gridding accounts for the fact that the data we combine are from different time periods with different dipole tilts. First, we take the median of the magnetic field strength at an arbitrary point in geodetic coordinates. We choose a latitude of 60° and longitude of 0° and 0km altitude for all our input data and calculate the median of the magnetic field strength at this point using the AACGM-v2 library. Once we have calculated all the magnetic field values for all input timeperiods, we then choose the date which is equivalent to the closest match of the median magnetic field strength. We then use the new date when specifying the magnetic field at each measurement location. This forms our new quasi-magnetic local time onto which we grid the data. For the gridding we use the same method as Ruohoniemi and Baker (1998). The gridding allows us to combine data from different time periods and specifying the most suitable dipole tilt as well as an appropriate magnetic field vector, similar to the method used by Thomas and Shepherd (2018).

In step 5, Fig. 2, we use a method similar to the 'MERGE' technique (Cerisier & Senior, 1994). The technique we use merges the vectors using an expansion of the standard SuperDARN technique. The 'MERGE' algorithm was developed to combine two LOS measurements from two overlapping radars' field-of-view to produce a single vector per grid cell. Our merging performs a least squares linear regression to each grid cell, assuming that the LOS velocity magnitude variation with respect to the azimuthal direction should be a cosine, and hence fit a cosine to the LOS magnitude variation with respect to the azimuthal direction. An example of this method is shown by Ruohoniemi and Baker (1998) in plates 3 and 4. Our method extends the original technique to combine as many measurements as are available per grid cell, instead of just two. Similarly to Thomas and Shepherd (2018), our merging vectors have to satisfy a minimum azimuth separation of 25°, but unlike Thomas and Shepherd (2018), we do not impose a minimum number of vectors per grid cell. Instead, we merge vectors wherever possible but if there is only one measurement, we keep the single LOS vector, which avoids gaps in the coverage. In the same way as Thomas and Shepherd (2018), we retain an error assigned to each grid cell: This is calculated as the mean of the input velocity vector errors in that cell.

For mode 1 and mode 3, most bins have over 4000 vectors and good spatial coverage but for mode 2, the number of vectors tends to be between 2000 and 3000. Due to the chosen time period for mode 2, the number of radars is reduced in comparison to mode 1 and 3, so the spatial coverage is not as good. Nevertheless, it is still way in excess of the ∼200 vectors shown by Walach, Grocott, Staples, and Thomas (2022) to be required for a well-constrained fit.

To be able to find the best fit global solution for the electrostatic potential from the merged vectors, we need to specify the lower latitude boundary, the HMB. This is done in step 6, Fig. 2. First we discuss this for mode 1 and then 2 and 3. To avoid the risk of a single-point failure in the automated detection algorithm adversely affecting the TiVIE results for mode 1, we do not apply the usual method of finding the HMB from gridded data that was described in section 2.1, which does not always work for statistical analyses, as discussed by Thomas and Shepherd (2018) and further below. Instead we use information from a statistical analysis of all 2-minute SuperDARN intervals contributing to a given TiVIE map to determine the HMB. The statistical distribution of HMB data was collected in step 4, alongside n, the number of LOS measurements per map. We choose the mean HMB location for the 20% of input maps (i.e. the data ingested in step 4) with the highest number of backscatter vectors. The 20% was an arbitrary choice that provided a stable result whilst minimizing a regression to the mean effect.

Similarly, when finding the HMB for modes 2 and 3, the traditional HMB-finding algorithm often places the HMB too high and produces unphysical results. The method used for mode 1 does not work as well for mode 2 due to fewer data points in some of the bins. An analysis of the HMB distributions found that the the median tends to place the TiVIE boundary too high, whereas the lower quartile value provides a good fit for substorms and geomagnetic storms alike (Walach et al., 2021). Walach and Grocott (2019) show the HMB distribution for geomagnetic storms (e.g. Figures 5 and 8) and Walach et al. (2021) found the HMB distribution is not symmetric about the median value. Consequently, the lower quartile of the HMB was used. We find a similar asymmetry for substorms and therefore use the lower quartile of the HMB distribution with respect to time, to determine the HMB in mode 2 and mode 3. Whilst this appears arbitrary as a choice, the HMB placement was based on the results by Walach and Grocott (2019); Walach et al. (2021) and is less arbitrary than choosing by eye as was done by Thomas and Shepherd (2018). Furthermore, this choice of HMB is a variable that can be changed in future versions of TiVIE.

The shape of the HMB was determined by Shepherd and Ruohoniemi (2000) and is indented to be more oval and located more poleward on the dayside than on the nightside. Once the HMB is chosen, we infill this dayside region where the HMB is indented with zero velocity vectors. This method was also used by (Thomas & Shepherd, 2018; Walach et al., 2021) to ensure the potential does not overreach the dayside HMB (some diffusion of the spherical harmonics is expected but we want to keep this to a minimum).

In step 7, Fig. 2, we apply the spherical harmonic analysis which produces the fitted electric potential maps. This method is the same as in the standard SuperDARN data processing technique developed by Ruohoniemi and Baker (1998). Here, the electrostatic potential distribution across the MLAT/MLT grid is calculated from the fitted velocity vectors using the equations $\mathbf{v} = \mathbf{E} \times \mathbf{B}/B^2$ and $\mathbf{E} = -\nabla\Phi$. The main difference to the usual SuperDARN processing technique outlined in section 2.1, is that we do not need a background model due to the high spatial coverage of vectors. We specify a sixth order expansion and the spherical harmonic fitting in the RST software finds a solution for Φ that best fits the vectors in each map. The final product is the electric potential maps, which are specified by the coefficients in the spherical harmonic expansions. The resulting maps for all three modes are available to download (Walach & Grocott, 2024b). The model is defined in the form of an electric potential map, but the electric field can in principle be readily computed from the resulting patterns.

TiVIE is very versatile and can produce modelled convection patterns for essentially any specification of input parameters (as long as this provides sufficient intervals of SuperDARN data for fitting). However, running the TiVIE model requires access to the fitted SuperDARN data archive and the SuperDARN analysis software RST. We therefore also provide a "TiVIE light" version of the model, that consists of model outputs for the set of predefined TiVIE runs which we present in this paper (TiVIE version 1.0). This is outlined by an optional step 8 in Fig. 2, which highlights our TiVIE light software package in the Python programming language (Walach & Grocott, 2024c). Alongside the TiVIE outputs (Walach & Grocott, 2024b) and the supplementary TiVIE light data (Walach & Grocott, 2024a), it can be used to produce individual convection maps and timeseries such as the ones we will showcase in the following sections. In specifying the input parameters, consideration has to be given to the probability of such conditions being met such that sufficient SuperDARN data are available to construct a convection map. For a sixth order expansion, the number of vectors required in principle to constrain a map is only 49 (Walach, Grocott, Staples, & Thomas, 2022), although the spatial distribution of the measurements is also critical (e.g. Walach, Grocott, Staples, & Thomas, 2022). Only by inspection can it be readily determined if sufficient data are available to produce a reliable map, but owing to the fact that coverage is uneven and patchy, the number of vectors is likely to be of the order 1000 or more. When the number of individual intervals available for the chosen TiVIE mode exceeds 5000, the number of data that are combined are truncated, such that they are limited to 5000 randomly chosen 2-minute input convection map intervals. Furthermore, similar to Cousins and Shepherd (2010) or Thomas and Shepherd (2018), it would also be possible to produce discrete maps and interpolate between the coefficients but this is not currently implemented in TiVIE.

Whilst we already mentioned that other convection models with parametrized maps exist, there are a number of advancements that the TiVIE model provides: 1) Mode 1 provide convection maps that not only reflect the IMF magnitude and clock angle but also the solar wind steadiness timescale, which is a novel addition. 2) Modes 2 and 3 provide the evolution of a substorm and geomagnetic storm, respectively. Other existing models do not explicitly capture the time evolution. 3) Modes 2 and 3 work when there are gaps in the solar wind measurements. This provides a clear benefit over existing models, for substorms and geomagnetic storms. We show examples of the modes and their benefits in the following sections.

To supplement the examples in the following sections, we show in the Supporting Information histograms of the Euclidian distances between model vectors and the merged vectors. We compare each map shown in this paper and compare the long τ data with short τ data, as well as long τ data with long τ model. For the substorm and storm modes, we compare the Euclidian distances between merged vectors and model vectors at onset, as shown in the manuscript and we compare these to the Euclidian distances between the merged vectors and the southward IMF model. In the supporting information, we also quote the mean of each distribution. In all cases in the SI, we clearly show that the

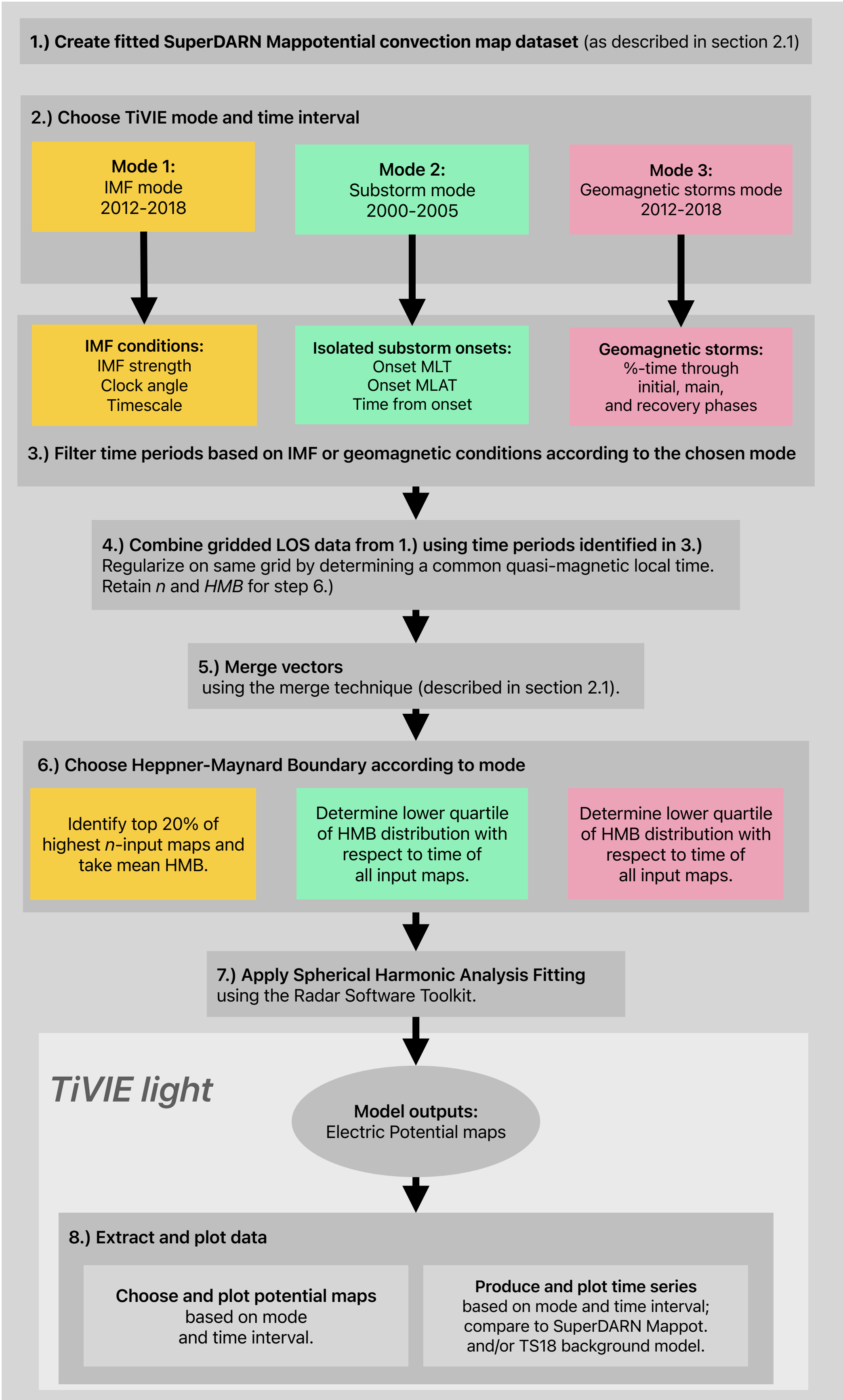

Figure 2. Flowchart illustrating the TiVIE model processing. See text for further discussion and explanation of the different steps.

introduction of a long τ criteria provides an improvement to the fitting, as well as substorm and storm binning.

3 Results

3.1 TiVIE Mode 1: Solar Wind Timescales

Figure 3 presents an example pair of TiVIE maps produced running mode 1. In this case, the electric potential has been parameterized using the IMF magnitude ($\geq 10\,\text{nT}$), clock angle ($-92.5° < \theta < -42.5°$), and steadiness timescale, τ_B. For the map on the left the τ_B parameterization is $20' < \tau_B < 30'$ and on the right it is $\tau_B > 360'$. The thick black lines and thick black dashed lines show the equipotential lines. The blue to red shading illustrates the electric potential strength. The grey dots indicate grid points where the model is constrained by data. The green line shows the convection map boundary (HMB), which is located just above 60° of geomagnetic latitude in both cases. n indicates the number of constraining vectors, which are 5689 (left) and 2572 (right). The cross polar cap potential Φ_{CPCP} shows the magnitude of the difference between the minimum and maximum equipotentials and is a measure of overall convection strength. Φ_{CPCP} is 31.53 and 42.76kV, respectively for the map on the left and right. Clear differences are apparent in the two patterns. The left-hand pattern is similar in morphology to the negative IMF B_Y pattern from Ruohoniemi and Greenwald (2005), in which they imposed a fixed 36 min steadiness criterion on the solar wind conditions (we compare to their 5-10nT, as this is their highest IMF strength bin). It also strongly resembles the negative IMF B_Y pattern from Thomas and Shepherd (2018) for a small solar wind electric field ($1.6 \leq E_{SW} < 2.1$ mV/m). The right-hand pattern of Fig. 3, on the other hand, displays a much stronger asymmetry between the dawn and dusk cells, with the dawn cell shrinking in size and, and the dusk cell both stronger, and extended and rotated such that it spans a wider range of local times, crossing both the midnight and midday meridians. Neither Ruohoniemi and Greenwald (2005) nor Thomas and Shepherd (2018) are able to reproduce this asymmetry due to their lack of binning by τ_B.

The $\tau_B > 360'$ map (right panel) shown in Figure 3 resembles previously reported observations of so-called TRINNI (Tail Reconnection during IMF-Northward, Non-substorm Intervals) flows (Grocott et al., 2005; Milan et al., 2005; Grocott et al., 2007). An example interval of data corresponding to the conditions of the right-hand panel in Fig. 3 is shown in Figure 4. In Fig. 4, n is 263, and these vectors are all concentrated around the nightside as shown by the pink vector scale. The black lines are showing the electrostatic potentials, for which the total magnitude difference from minimum to maximum is given by Φ_{CPCP} as 34.66kV. The green line is showing the HMB. In this pattern, the dawn cell is largely missing, and the dusk cell is extended in local time across the midnight meridian. The IMF clock angle during this interval was $\theta \simeq -70°$ and the magnitude was $\sim 10\,\text{nT}$, putting it within the ranges used to parameterize the model maps in Fig. 3 (right). In this case the IMF conditions during this interval had been relatively steady, within the range for $\tau_B \sim 6$ hours. The convection map in Fig. 4 shows clear evidence for the importance of τ_B, being appreciably different from the pattern in Fig. 3 (left). Conversely, it appears to show that TiVIE is remarkably good at capturing the morphology of the electric potential under these conditions. This map is from 1999 and these data were not included in TiVIE, so this shows that the model is consistent with the expected convection map morphologies.

3.2 TiVIE Mode 2: Substorms

A number of previous studies have demonstrated that substorms can have a substantial impact on the morphology of the ionospheric convection pattern (e.g. Provan et al., 2004; Grocott et al., 2002, 2006, 2009, 2010; Grocott, 2017). In particular, it has been shown that the latitude and local time of substorm onset are key factors in con-

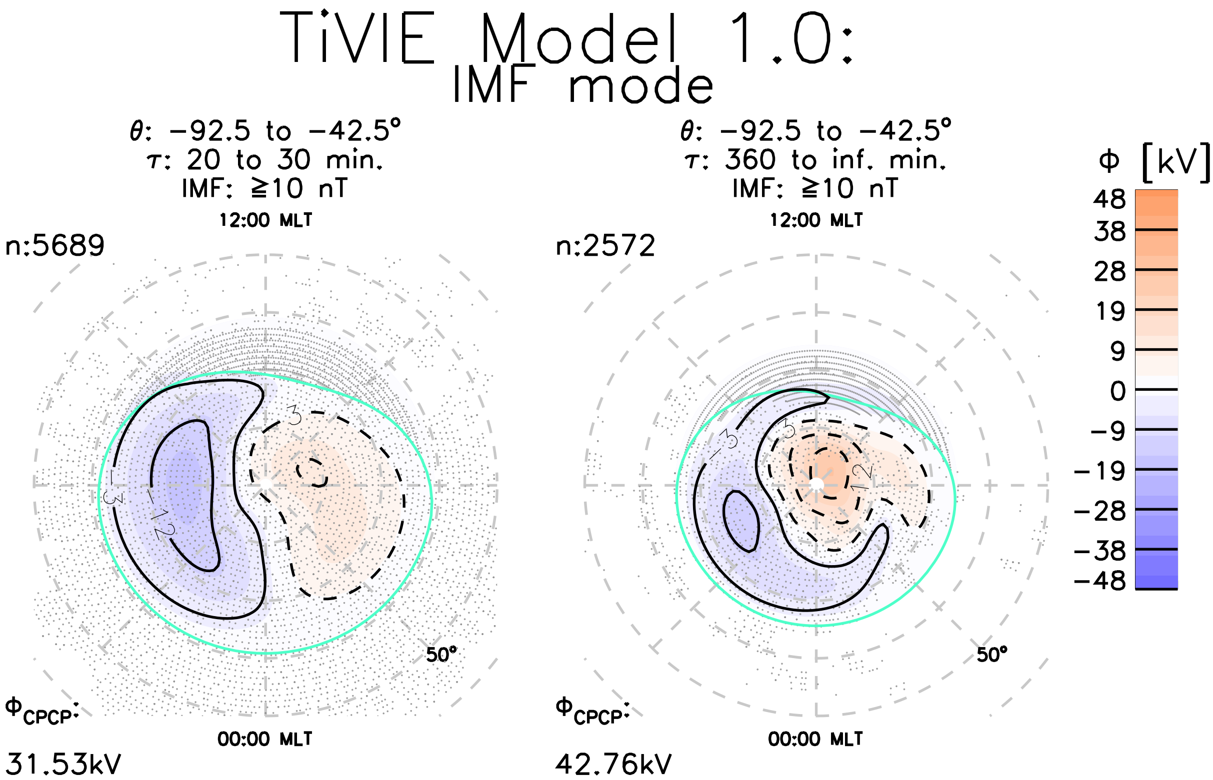

Figure 3. Two example electric potential patterns in AACGM-v2 coordinates for TiVIE mode 1. The IMF clock angle bin is $-92.5^\circ < \theta < -42.5^\circ$ and the magnitude bin is $\geq 10\,\mathrm{nT}$. The map on the left corresponds to an IMF steadiness timescale $20' < \tau_B < 30'$ and on the right $\tau_B > 360'$. The thick black lines and thick black dashed lines show the equipotential lines. The colours (blue to red) illustrate the electric potential strength. The grey dots indicate grid points where the model is constrained by data. The green line shows the convection map boundary (HMB). n indicates the number of constraining vectors and Φ_{CPCP} shows the magnitude of the difference between the minimum and maximum equipotentials.

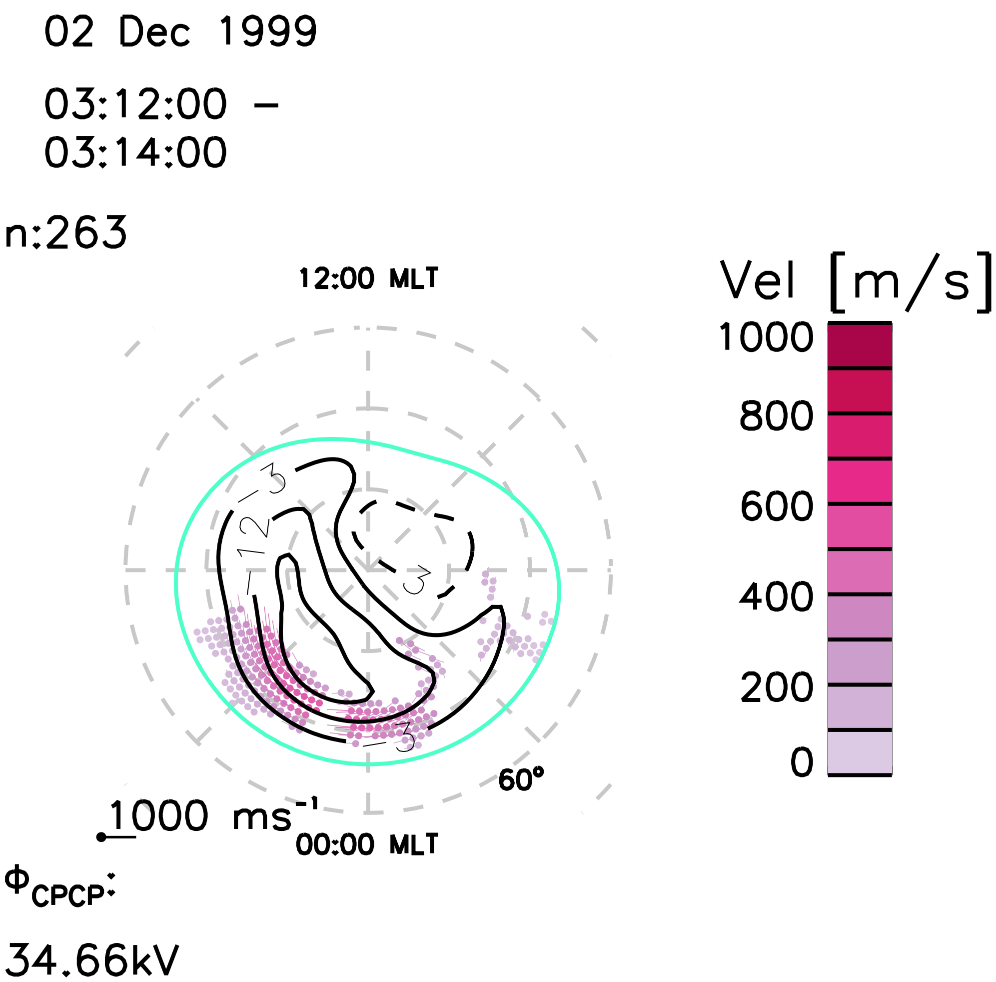

Figure 4. An example 2-min SuperDARN convection pattern in AACGM-v2 coordinates from 03:12 to 03:14 UT on 2nd December 1999. Flow vectors are shown by the pastel pink to bright pink vectors, where gridded radar data were available during the 2-min interval. The black vector in the bottom left shows a fast flow vector for scale. The black contours represent the electric equipotentials and the green line represents the convection map boundary (HMB). n indicates the number of constraining vectors and Φ_{CPCP} shows the magnitude of the difference between the minimum and maximum equipotentials.

trolling the substorm influence. Grocott et al. (2009) showed that the convection pattern size and transpolar voltage increases with lower latitudes of onset locations. Grocott et al. (2010); Grocott (2017) on the other hand, showed that the location of the convection reversal is dependent on the onset local time. Depending on the nature of any particular use case for TiVIE, it might therefore be desirable to have a choice of substorm onset bins. Here, we show parameterizations focussing on either the MLT or the latitude of onset to ensure reliable coverage is kept. Figure 5 presents four examples of TiVIE maps produced running 'substorms' mode 2. In all cases, the electric potential has been parameterized by the time relative to substorm onset ($0-2$ mins), but we show two examples of different onset bins for the substorms here: The top row shows a static MLT band (20:00 to 03:00 MLT) for onset and a varying magnetic latitude (59 to 61° and 67 to 68°, respectively). The bottom row shows a static magnetic latitude range (64 to 69°) and a varying MLT range (00:00 to 02:00 and 20:00 to 22:00 MLT, respectively). Each map is in AACGM-v2 coordinates and the black (dashed) lines show the equipotential contours. The blue to red shading shows the electrostatic potential and the HMB is shown by the outer green boundary. The boundary for possible onset locations in each case is shown by the outlined area in green, using observations from the Frey et al. (2004) list. In the bottom row the magnetic latitude range is slightly larger, which is to ensure that the number of substorms is similar for all four configurations. n is high (above 2000) for all maps and the grey dots show the distribution of constraining vectors, which are well spread out. The magnitude of the difference between the minimum and maximum equipotentials, Φ_{CPCP}, is ∼30-40kV for all maps, except for the top left map, where Φ_{CPCP} is much higher at ∼58 kV. This can be explained due to the onset location, which is at a lower latitude than the other convection maps and implies that the substorm growth phase was larger. Clear similarities and differences are apparent between the four patterns. For the top row, the primary difference lies in the size of the pattern and the transpolar potential: Substorm onsets which occur at a lower magnetic latitude lead to a larger pattern, but also a higher transpolar voltage. When we specify substorm onsets with a stricter MLT range but keep the magnetic latitude static (see bottom row), Λ_{HMB} and Φ_{CPCP} are more similar but the convection pattern changes shape: When the substorm onsets are located post midnight (bottom left), the convection pattern is such that the onset location is overlapping with the flow reversal region on the nightside. When the onsets are located in the pre midnight sector (bottom right), the convection cells are rotated, such that the flow reversal region lies in the pre midnight sector. In this case, the flow reversal region does not fully align with the onset region.

Grocott et al. (2010) also produced average substorm patterns, which looked similar to our bottom two rows of Fig. 5. They chose a single onset latitude bin of 65 to 67° and then subdivided by average IMF B_Y conditions: This yielded an onset pattern similar to the two in our bottom row with the convection reversal on the pre midnight side for positive IMF B_Y and the convection reversal on the post midnight side for negative B_Y at onset. Since we did not subdivide our substorm categories by IMF conditions, we do not expect the patterns to be identical. For example, Grocott et al. (2010) found the mean substorm onset location for negative B_Y to be sitting on the duskside edge of the convection reversal boundary, whereas our convection reversal location for the pre-midnight onsets does not fully overlap with the onset location, as discussed above. Our substorms not being sub-divided by IMF conditions could be a reason for this difference. Another reason could be the fact that the dusk cell generally dominates the convection pattern: Walach, Grocott, Thomas, and Staples (2022) showed that the dusk cell dominates 77% of all time during the years 2010 to 2016. Further differences between our processing methods and those of Grocott et al. (2010) are also likely to be contributing. Grocott et al. (2010) used an older version of the SuperDARN data processing algorithm (e.g. FitACF version <2.5, whereas we used version 2.5) and they also did not use a range limit when ingesting radar data.

Both substorm binnings (wider MLT bin or wider MLAT bin) are available, but which one is used is up to the individual user: A narrower MLAT bin provides a more reliable HMB but comes with a wider MLT bin and therefore the nightside convection reversal region is more smoothed, whereas a wider MLAT bin and a narrower MLT bin provides a better parameterization of the nightside convection reversal region, but a less accurate HMB location, so there is a trade-off. Ideally, we would have a bin that is narrow in MLT and MLAT but the coverage would not be as good and result in fewer vectors being binned. Smaller bins would therefore mean a less accurate map overall and would be a more severe trade-off. Instead we have provided the user with options, depending on their needs.

Figures 6 and 7 show an illustrative example of TiVIE mode 2 in action for the substorm onset at 04:18UT on 26^{th} December 2000. Figure 6 shows a convection map of the substorm onset time. The timeseries of this is shown in Fig. 7 by the purple lines in the last few panels. The convection map is in AACGM-v2 coordinates and the electrostatic potentials are shown in black. The green boundary indicates the HMB. The map shows that n is high (363) and well-distributed across almost all MLT sectors. The vectors are shown in pink and are mostly quite light, indicating that the plasma is fairly slow moving. This substorm's onset occurred at a latitude of 67 to 68° and an MLT of around 23:30 as indicated by the cross in Figure 6. Comparing the convection map in Fig. 6 with Fig. 5, our onset location would match the top right bins, but the convection morphology is most similar to the binning on the bottom right. For the example on the bottom right in Fig. 5, we used the early-midnight onset bin described earlier and our example in Fig. 6 is just outside this bin, but at a similar magnetic latitude. This means that this particular substorm was not included in the binning of the substorms in the bottom right in Fig. 5 and serves as a simple validation test. The similarity between Fig. 5 and Fig. 6 shows that the substorm binning reproduces the same morphologies and is representative of this substorm example. Φ_{CPCP} is also comparable for both the convection map in Fig. 6 (35.15 kV) and the bottom right binning in Fig. 5 (37.48 kV). The top right binning in Fig. 5 is also comparable with (31.76kV) but because it is a broader bin in MLT, the morphology is less similar.

Fig. 7 shows a timeseries of the previously mentioned isolated substorm with the vertical black dashed line denoting onset. The timeseries shown encompasses the time period 02:18 UT to 06:18 UT on 26^{th} December 2000. The first two panels show the IMF components, and the solar wind speed which indicate that there is enhanced solar wind driving. The third and fourth panels show the geomagnetic conditions: AU and AL, which indicate an isolated substorm, and the Sym-H index, which indicates little intensification of the ring current and hence no geomagnetic storm activity. The next three panels show a comparison between TS18 model (bright pink), TiVIE mode 1 (light pink), TiVIE mode 2 (light green), and the SuperDARN convection maps, labelled as Mappotential (purple). For TiVIE mode 2, we show the bin in which our substorm onset falls in, which is the wider MLT binning and higher latitude range (e.g. top right panel in Fig. 5). The fifth panel shows the transpolar voltage (Φ_{CPCP}), which increases slightly prior to substorm onset (from ∼3:40 UT) for TiVIE mode 2 and the SuperDARN maps. The TS18 model and TiVIE mode 1 on the other hand show the electrostatic potential peaking around an hour before substorm onset when the solar wind driving is higher. We also see the TS18 Φ_{CPCP} dropping after onset, which is associated with the increase in IMF B_Z, whereas both the SuperDARN maps and the TiVIE Φ_{CPCP} remain elevated. We speculate that this is due to ongoing driving from the magnetotail, which TS18 does not capture. The latitude of the HMB, is very similar for the SuperDARN maps, TiVIE mode 1 and 2, whereas Λ_{HMB} is a little more variable for TS18. The changes in the HMB for TiVIE are almost the same for all data shown: We see a small decrease (towards the equator) during growth and increase (towards the pole) during expansion/recovery of a degree or so, which is in agreement with the ECPC model. The sixth panel shows the number of data points for the maps and whilst it is much lower for the SuperDARN maps,

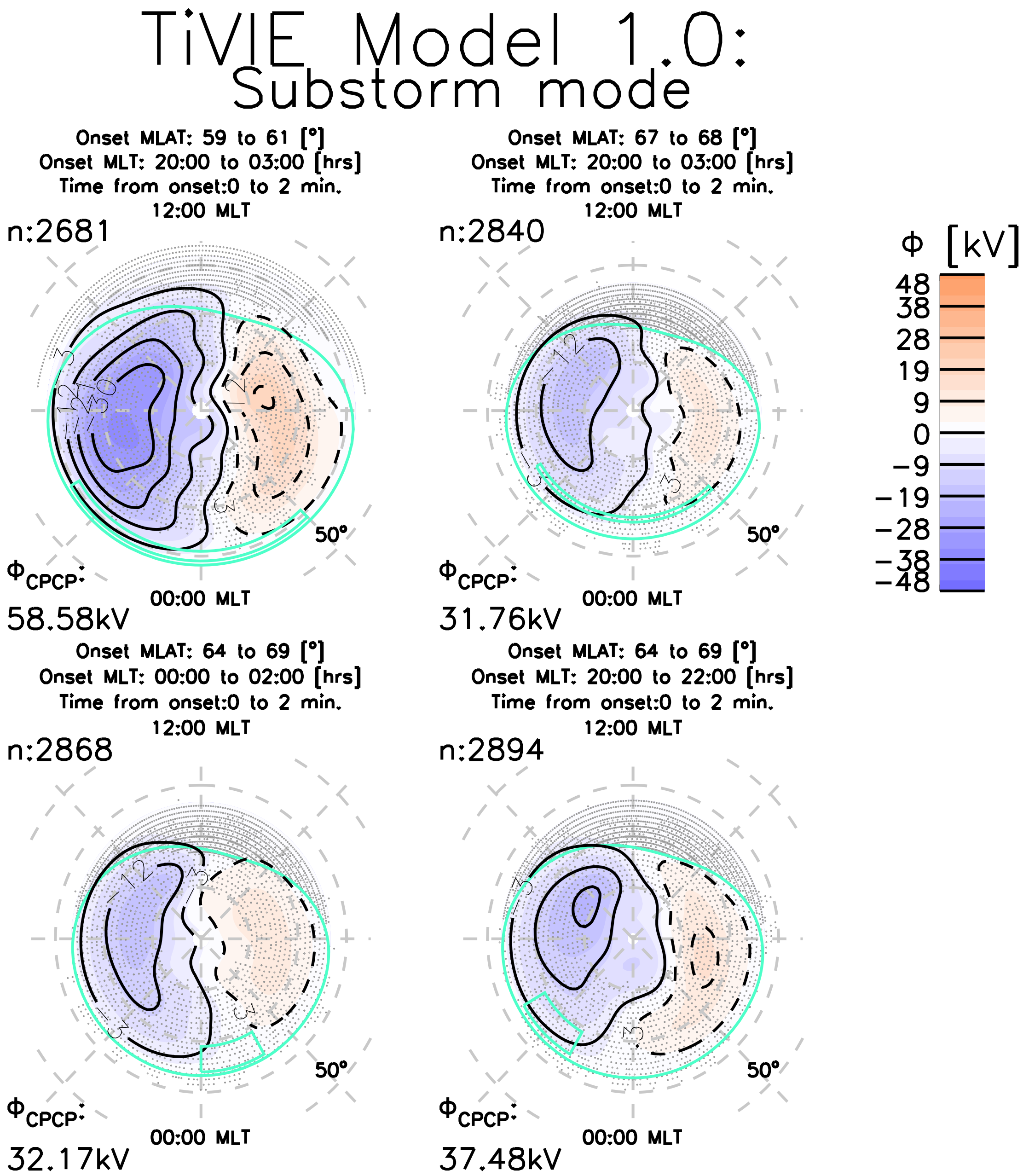

Figure 5. Four example electric potential patterns in AACGM-v2 coordinates for TiVIE mode 2. In all cases the maps are comprised of data from the 2-min interval following the onset. The top row shows substorms observed between 20:00 and 03:00 MLT and the bottom row shows substorms, which have a narrower MLT occurrence bin: between 00:00 and 02:00 MLT (bottom left) and 20:00 and 22:00 MLT (bottom right). The magnetic latitudes of onset were 59 to 61° (top left) and 67 to 68° (top right) and 64 to 69° (bottom row). The onset region is marked by the green band and the HMB is also shown in green. The thick black lines and thick black dashed lines show the equipotential lines. The colours (blue to red) illustrate the electric potential strength. The grey dots indicate grid points where the model is constrained by data. n indicates the number of constraining vectors and Φ_{CPCP} shows the magnitude of the difference between the minimum and maximum equipotentials.

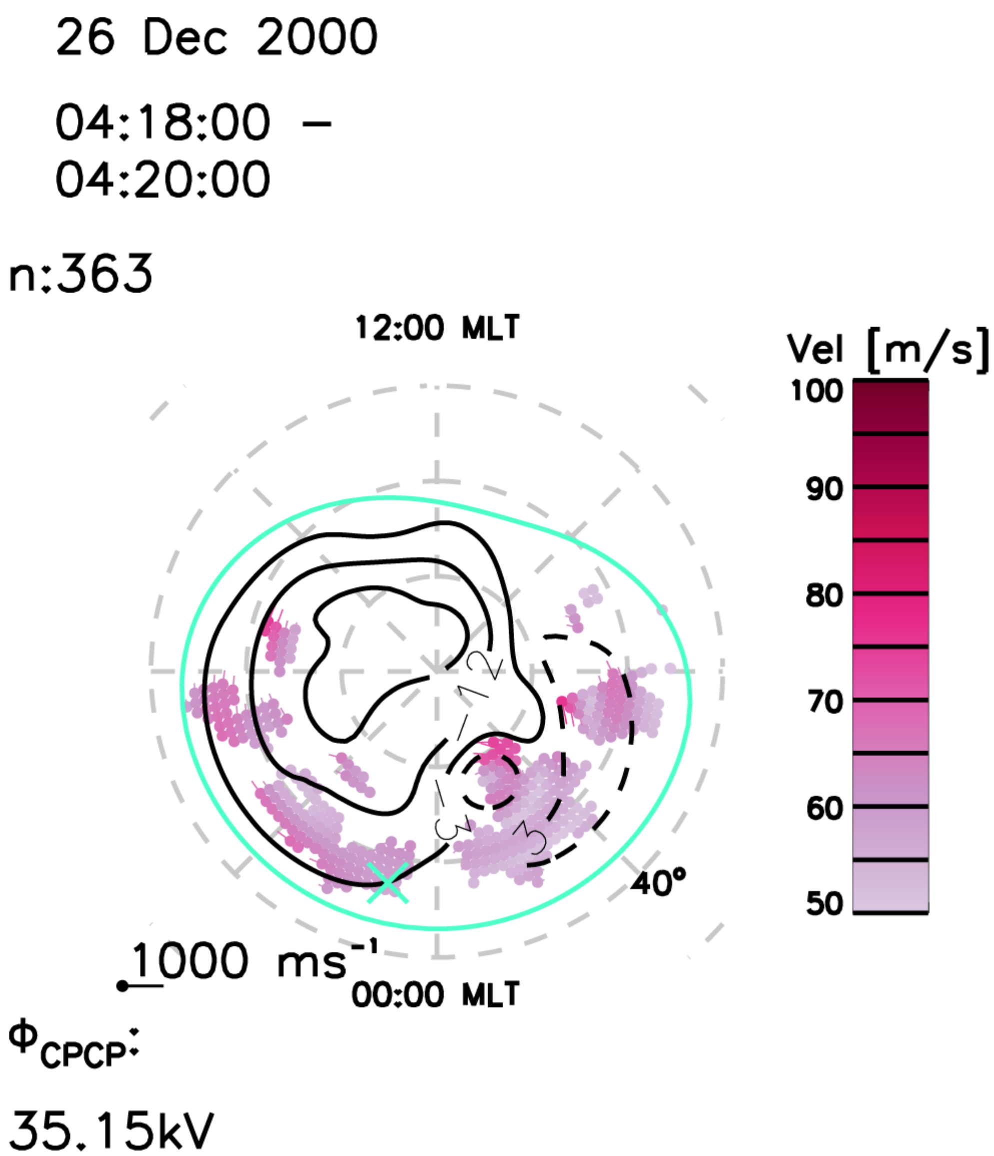

Figure 6. An example electric potential patterns for a substorm onset in AACGM-v2 coordinates. The map shows the SuperDARN map at onset time from Fig. 7. The green cross indicates the substorm onset location (left map). The flow vectors are shown by the pink scale. The bottom left shows a black vector scale for the plot on the left. The thick black lines and thick black dashed lines show the equipotential lines. The green line shows the convection map boundary (HMB). n indicates the number of constraining vectors and Φ_{CPCP} shows the magnitude of the difference between the minimum and maximum equipotentials.

n remains above 200 for the entire interval. Whilst the TiVIE model is constructed with many more data points ($\sim$times a factor of 10), 200 data points is still considered good number for any individual map (Walach et al., 2021).

3.3 TiVIE Mode 3: Geomagnetic Storms

Figure 8 presents three example TiVIE maps in AACGM-v2 coordinates, produced running 'geomagnetic storm' mode (3). In this case, the electric potential has been parameterized by the time relative to the start of each storm phase as described in section 2.2. In this example, we use no further parameterizations, which means this mode is immune to gaps in IMF data, like the mode 2. This makes sense in practise as it provides a way of assessing and capturing the variability more directly associated with storm evolution, as shown by Walach et al. (2021). Each map shows the equipotentials with black lines and the blue to red shading indicates the electric potential. The grey dots show the location of the constraining vectors and the green boundary shows the HMB.

The maps in Figure 8 correspond to the start of each phase, which is (from left to right) the initial, main and recovery phase. The three patterns reveal clear differences, however, in order to demonstrate the relevance of such a parameterization and its value in TiVIE over existing solar wind parameterized models, we must still consider the IMF conditions in this case. We quickly summarise the average IMF conditions for the geomagnetic storms used here, which can also be found in Walach and Grocott (2019) and Walach et al. (2021)). Φ_{CPCP} increases from the initial (34.13kV) to the main phase (62.72kV) and then again to the recovery phase (79.02kV).The average IMF B_Y component is understandably fairly small for geomagnetic storms. The average IMF B_Z, on the other hand, becomes strongly negative during the storm parameterization used here, as all storms are strongly solar wind-driven times, and this is reflected in the average conditions captured by TiVIE here. In fact, at the start of the initial phase (left panel in Fig. 8), the IMF B_Z component is on average typically small, and consequently the resulting electric potential pattern is quite weak, and actually resembles a cross between the $B_Y >$ 0 and $B_Y < 0$ patterns for weak solar wind driving presented by Thomas and Shepherd (2018). The pattern for the start of the main phase (middle panel in Fig. 8), on the other hand, is much stronger, which is consistent with the fact that the IMF B_Z component is on average $-4\,\mathrm{nT}$ at this time during a prototypical storm. The more interesting result is that revealed by the third pattern (right panel in Fig. 8), from the start of the recovery phase. The average IMF B_Z component for a geomagnetic storm is $-4\,\mathrm{nT}$ at this time, the same as for the main phase, yet the pattern is clearly larger in size, having expanded from a HMB of 53° down to 50° magnetic latitude. This implies that a simple IMF parameterization would be inappropriate for geomagnetic storms.

It is worth considering that during the main phase of a geomagnetic storm, the average IMF B_Z component remains negative (e.g. see Walach and Grocott (2019) and Walach et al. (2021)). Thus, an alternative way of parameterizing the storm-time behaviour might be to use TiVIE mode 1, with an appropriate τ_B. For the storms used to parameterize TiVIE here, the median main phase duration was ~ 9 hours. Performing TiVIE model 1 runs, with IMF $B_Y = 0$, $B_Z = -4\,\mathrm{nT}$ and $20' < \tau_B < 30'$ for the first run and $240' < \tau_B < 360'$ for the second, yields the results shown in Figure 9. These show two convection maps for the chosen TiVIE mode using the same layout, colour-coding and coordinates, as previous TiVIE convection maps. The mode 1 examples in Figure 9 and mode 3 patterns in Figure 8 look quite similar. But here we also see the effects of prolonged strong solar wind driving, with the convection pattern expanding from 53° down to 43° magnetic latitude, whereas for the beginning of the recovery storm phase, Λ_{HMB} only reaches 50°. Furthermore, we see in the right panel in Fig. 9 that when the solar wind driving is prolonged, the dusk convection cell drapes across the nightside meridian, which is a less pronounced feature in geomagnetic storms. Whilst the HMB latitude of the pattern on the right in Fig. 9 is lower than for the beginning of the recovery phase,

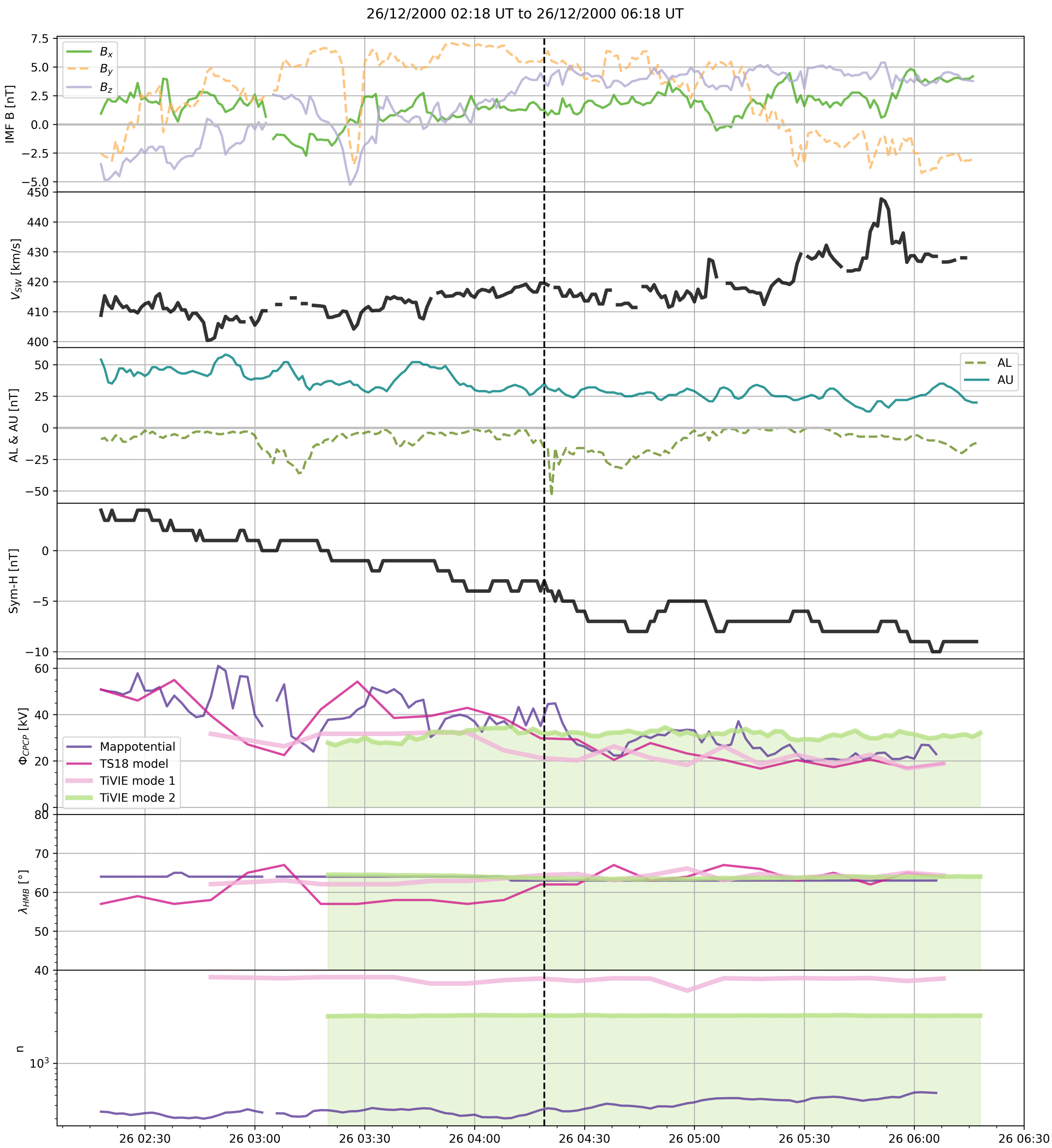

Figure 7. A summary plot showing TiVIE mode 2 in action for the time period 02:18 UT to 06:18 UT 26th December 2000. The panels show the IMF components, the solar wind speed, the AL and AU indices, the Sym-H index, the transpolar voltage (Φ_{CPCP}), the latitude of the Heppner-Maynard boundary (Λ_{HMB}), and number of data points per map (n). For the last three panels, we show the TS18 model (bright pink), the TiVIE mode 1 (light pink), TiVIE mode 2 (light green), and the SuperDARN maps, labelled Mappotential (purple). The vertical dashed black line shows the substorm onset at 04:18 UT on 26th December 2000. Substorm onset occurred at a latitude of 67 to 68°.

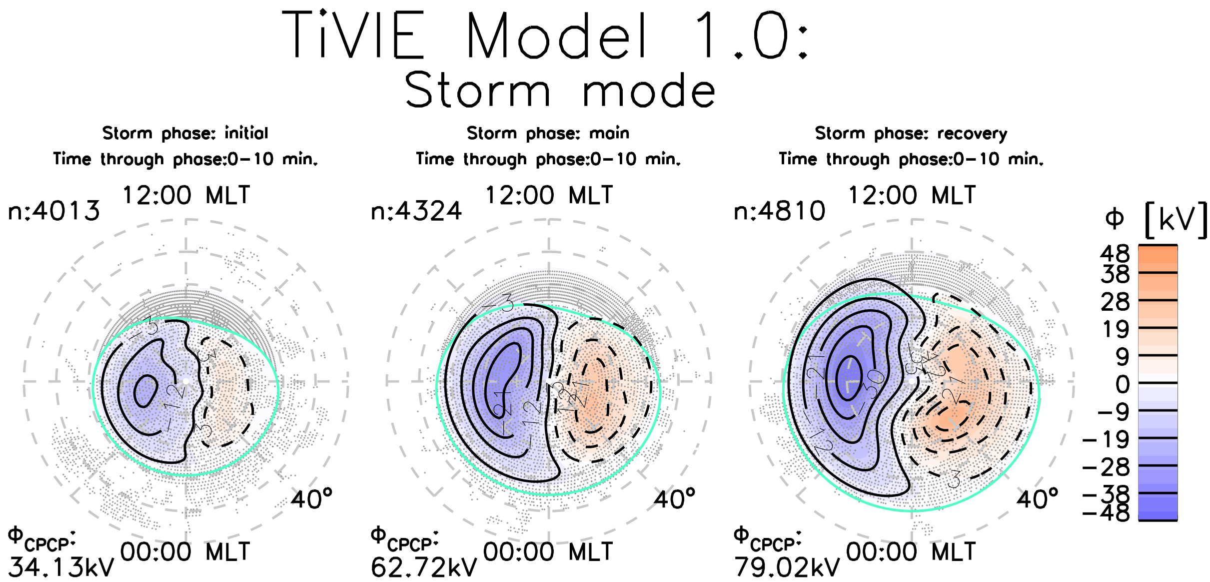

Figure 8. Three example electric potential patterns in AACGM-v2 coordinates for TiVIE mode 3, corresponding to the times of the start of each storm phase. From left to right, this is the initial, main and recovery phase. The storm phases were determined from the Sym-H index according to the method described by Walach and Grocott (2019). The thick black lines and thick black dashed lines show the equipotential lines. The colours (blue to red) illustrate the electric potential strength. The grey dots indicate grid points where the model is constrained by data. The green line shows the convection map boundary (HMB). n indicates the number of constraining vectors and Φ_{CPCP} shows the magnitude of the difference between the minimum and maximum equipotentials.

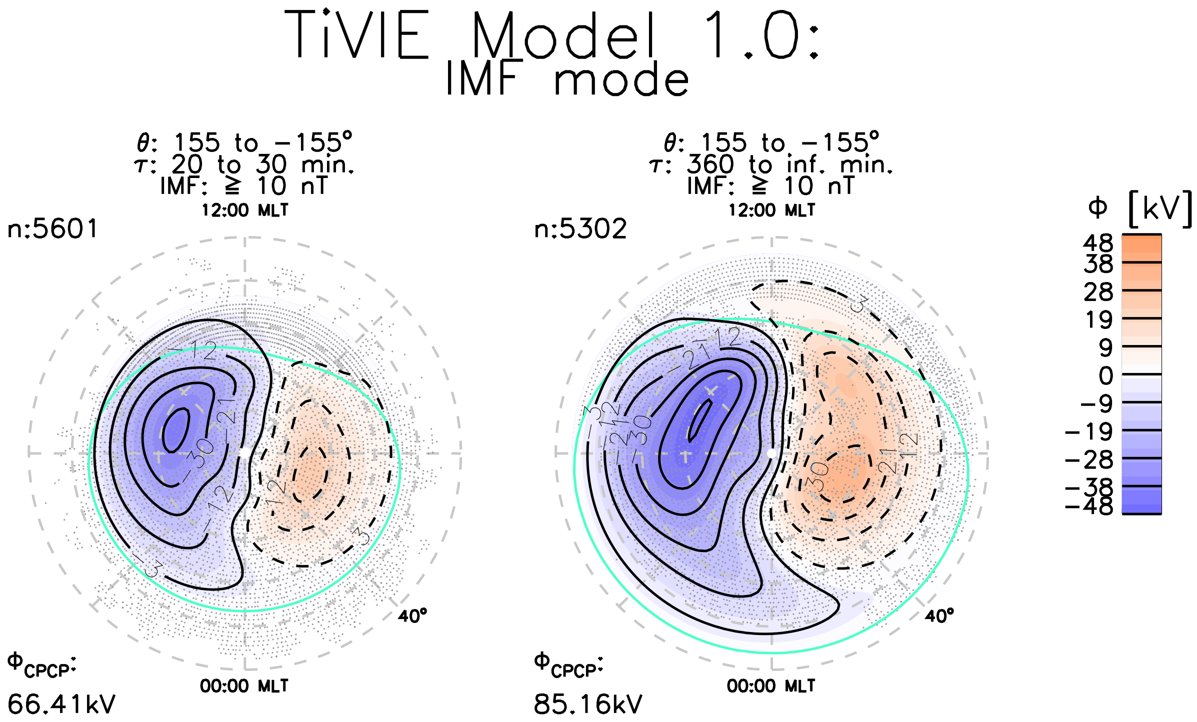

Figure 9. Two example electric potential patterns in AACGM-v2 coordinates for TiVIE mode 1. The IMF clock angle bin is $155^\circ < \theta < -155^\circ$ and the magnitude bin is $\geq 10\,\mathrm{nT}$. The map on the left corresponds to an IMF steadiness timescale $20' < \tau_B < 30'$ and on the right $\tau_B > 360'$. The thick black lines and thick black dashed lines show the equipotential lines. The colours (blue to red) illustrate the electric potential strength. The grey dots indicate grid points where the model is constrained by data. The green line shows the convection map boundary (HMB). n indicates the number of constraining vectors and Φ_{CPCP} shows the magnitude of the difference between the minimum and maximum equipotentials.

the IMF field strength is also higher. Walach et al. (2021) analysed the time variability of the storm time convection patterns and quantified the changes using a Principal Component Analysis. One of the findings from Walach et al. (2021) was that the storm time patterns, a key sample of which is shown in Fig. 8, show a time-variability in relation to the sun-midnight meridian alignment of the dayside convection throat. This feature is particularly visible in the Principal Component Analysis when the geomagnetic storm mode convection maps from the whole storm are analysed together. This is a morphological feature which the IMF mode maps do not always express (for the interested reader we recommend Fig. 8, which analyses these changes in more detail). These results show that there may be more than one TiVIE mode that can be used, and that which mode is chosen, might depend on the specific circumstances under investigation.

Figure 10 shows an example convection map, where the IMF has been strongly southward for a long time (several hours) and a geomagnetic storm occurs. The coordinates and colour-coding is the same as Fig.4: Flow vectors, where SuperDARN measurements are available are shown by the coloured dots. Λ_{HMB} is shown by the green coloured shape and the black contours represent the equipotentials. For this map, 637 flow vectors were available, which is an unusually high number of vectors. Furthermore, the vectors are well distributed geographically, as coverage is available across most nightsectors, from almost 15:00 to 03:00 MLT, and another patch of vectors is available near 09:00 MLT. In this example, the IMF has been southward for some time and we can see the convection map has taken on the shape of the map shown on the right side of Fig. 9 and the Φ_{CPCP} is similar too (albeit it is higher here with 112 kV instead of 85 kV). Fig. 10 particularly illustrates the way the dusk convection cell stretches across the midnight meridian, which we do not see for intervals of short southward IMF. It is worth noting however that Λ_{HMB} in Fig. 10 only reaches $\sim 50°$, making it more similar to TiVIE mode 3, as opposed to the TiVIE mode 1 shown in Fig. 9. Clearly, TiVIE modes 1 and 3 can produce similar Φ_{CPCP} and choosing the correct mode, may well be dependent on the context: Fig. 10 shows one snapshot in time, which agrees well with TiVIE mode 1, except for the Λ_{HMB}. In order to represent the geomagnetic storm well, however, mode 3 may be more appropriate as mode 3 incorporates the entire time-history of the geomagnetic storm and is not susceptible to gaps of solar wind data or lack in SuperDARN measurement coverage.

Figure 11 shows a timeseries for a geomagnetic storm during the time period 14:46 UT 6^{th} March 2012 to 10:48 UT 8^{th} March 2012. The panels are ordered in the same way as for Fig. 7. The vertical black dashed lines indicate the beginning of the main and recovery phases. We see that when the IMF B_Z component is negative, the Sym-H index decreases and the storm main phase in the TiVIE mode 3 causes Φ_{CPCP} to increase and then slowly decay again with the storm. When the storm main phase occurs, Λ_{HMB} for TiVIE mode 3 also moves to lower latitudes, which is mirrored by the instantaneous SuperDARN maps (Mappotential line), as well as TiVIE mode 1 and the TS18 model. We see that for this storm, the number of data points used to create the SuperDARN archive, n, is $\sim$500-1000 in the early hours of the storm, which is very high (Walach & Grocott, 2019; Walach, Grocott, Staples, & Thomas, 2022). Later, during the recovery phase of the storm when Sym-H is recovering from the decrease the n drops close to 0 for the SuperDARN maps, which illustrates a key issue that TiVIE is able to solve: The rapidly fluctuating n affects the quality of the instantaneous (Mappotential) convection maps and this is reflected in the abruptly fluctuating Φ_{CPCP} and Λ_{HMB}. Similarly, the TS18 model and TiVIE mode 1 completely drop out at times when no IMF information is available, whereas TiVIE mode 3 is much more stable: Both Φ_{CPCP} and Λ_{HMB} are much smoother for TiVIE mode 3 and it may therefore be a more appropriate model for geomagnetic storms. The fact that the geomagnetic storm mode can perform when no IMF data is available is a clear benefit of TiVIE over the TS18 model or similar models.

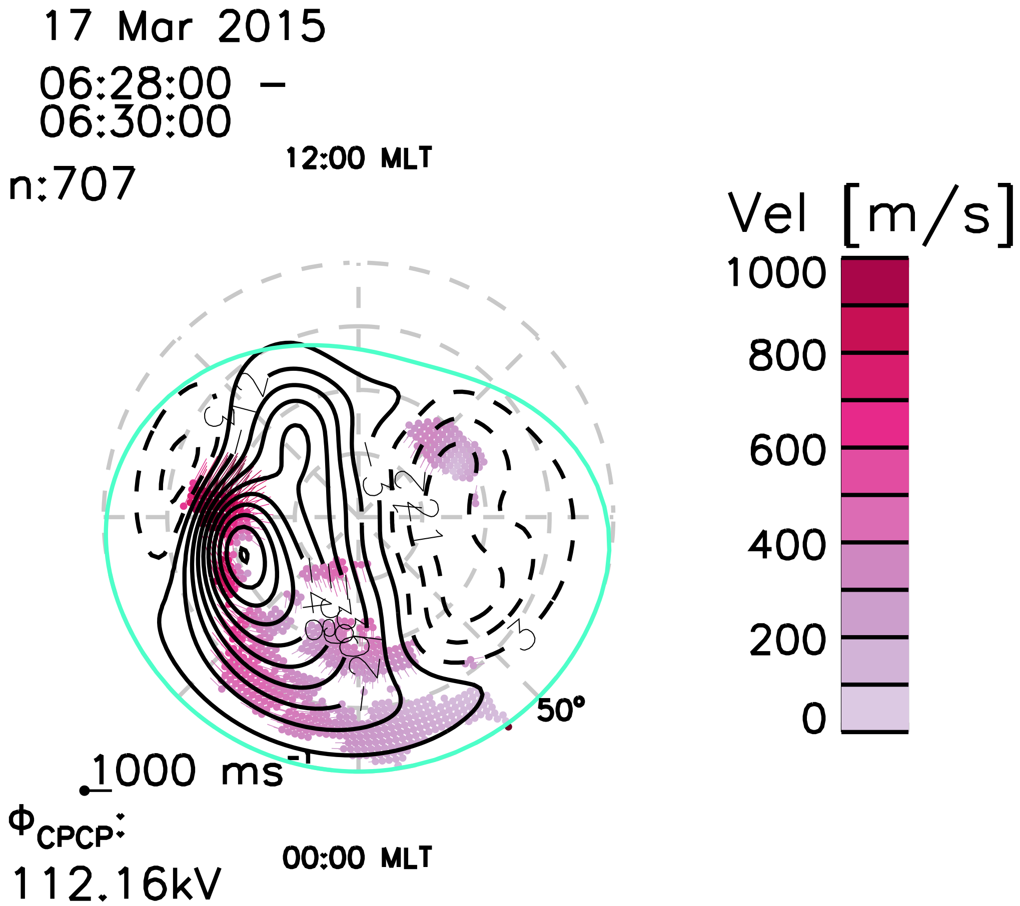

Figure 10. An example 2-min SuperDARN convection pattern from 06:30 to 06:32 UT on 17 March 2015 in AACGM-v2 coordinates. Fitted flow vectors are shown by the pink scale where gridded radar data were available during the 2-min interval. The black vector in the bottom left corner shows a scale for the vector length. The black contours represent the electric equipotentials and the green line represents the lower latitude boundary (HMB). The magnitude of the difference between the minimum and maximum potential is given by Φ_{CPCP} as 112.16kV and the number of vectors for this map was 707 (n).

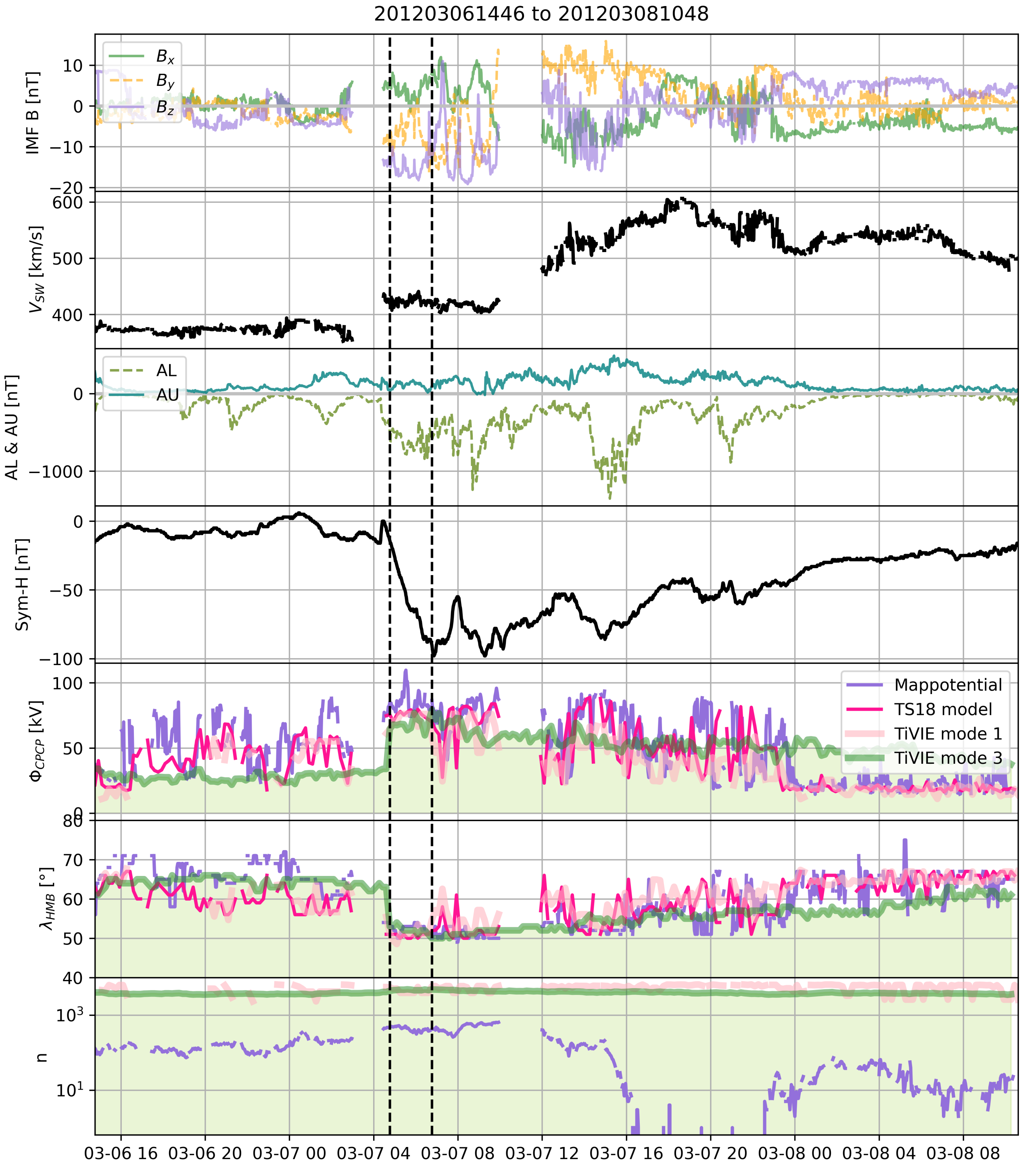

Figure 11. A summary plot showing TiVIE mode 3 in action for the time period 14:46 UT 6^{th} March 2012 to 10:48 UT 8^{th} March 2012. The panels show the IMF components, the solar wind speed, the AL and AU indices, the Sym-H index, the transpolar voltage (Φ_{CPCP}), the latitude of the Heppner-Maynard boundary (Λ_{HMB}), and number of data points per map (n). For the last three panels, we show the TS18 model (bright pink), the TiVIE mode 1 (light pink), TiVIE mode 2 (light green), and the SuperDARN maps, labelled Mappotential (purple). Dashed vertical black lines show the beginning of the storm main and recovery phases.

4 Summary and Conclusions

We have presented the details of, and initial results from, the Time-Variable Ionospheric Electric potential (TiVIE) model. TiVIE is designed to capture three major sources of time-dependence in the coupled solar wind-magnetosphere-ionosphere system. The first source of variability relates directly to the time-dependence of the system to the upstream solar wind conditions, specifically the interplanetary magnetic field or solar wind electric potential. To account for the evolution of the electric potential with time, we define a solar wind steadiness timescale with which we parameterize the electric potential. Using some examples, we show that the timescale can have a profound effect on the convection pattern, such as enhancing the transpolar voltage and convection strength to similar levels as those seen during geomagnetic storms. The second source of variability relates to the storage and release of energy in the magnetosphere that is associated with the substorm. The electric potential evolves throughout the substorm cycle, and its morphology is strongly influenced by the location of substorm onset. We show two parameterizations relative to substorm onset location, based on previous studies: One which prioritizes the magnetic latitude and one which prioritizes the magnetic local time of onsets. We show that these parameterizations are consistent with previous results (e.g. Grocott et al., 2009; Grocott, 2017), which have shown that convection pattern size and transpolar voltage increases with lower latitudes of onset locations and that the location of the convection reversal responds to onset locations. Lastly we account for the variability introduced by geomagnetic storms. The ionospheric electric potential evolves differently through each phase of a storm and this we account for by parameterizing the electric potential patterns by storm phase. During a geomagnetic storm, the convection pattern moves to latitudes as low as 50°. In this initial study, we present the first version of TiVIE, which allows us to interactively take into account the time-dependency of the system, which is a major development from previous models. We provide solutions to major challenges regarding data gaps: Whilst other models may depend solely on solar wind conditions, our TiVIE mode 2 and 3 mean that when a space weather event, such as a substorm or geomagnetic event occurs, a model output can still be produced, regardless of solar wind measurement gaps. Similarly, when SuperDARN suffers from low data coverage, which is out of our control, we can use TiVIE to produce a convection map that includes the time history of the solar wind-magnetosphere interactions.

Future developments may include further modes to encompass other types of geomagnetic activity, for example, steady magnetospheric convection events, sawtooth events and recurring substorms (e.g. Walach & Milan, 2015; Walach et al., 2017). Other avenues for future improvements could include the inclusion of a larger database, such that extreme conditions (e.g. higher solar wind strengths or extreme geomagnetic storms) are better represented, and the bins could then be fine-tuned and split further. Future studies are underway, which will validate TiVIE against existing models and datasets. TiVIE may be of particular interest to large-scale models, such as whole atmosphere models or space weather models, which rely on an ionospheric electric potential as input. In particular, we look to further validate the model and investigate the sensitivity of Whole Atmosphere Community Climate Model with thermosphere and ionosphere eXtension (WACCM-X) model (Liu et al., 2018) to the choice of input electric potentials derived from models during geomagnetic storms.

Open Research Section

The authors acknowledge the use of SuperDARN data. SuperDARN is a collection of radars funded by national scientific funding agencies of Australia, Canada, China, France, Italy, Japan, Norway, South Africa, United Kingdom, and United States of America, and we thank the international PI team for providing the data. The authors acknowledge access to the SuperDARN database via the British Antarctic Survey British Antarctic Survey (2017).The Radar Software Toolkit (RST) to process the SuperDARN data can be

downloaded from Zenodo (SuperDARN Data Analysis Working Group et al., 2018). All solar wind data and geomagnetic indices were downloaded from NASA's SPDF Coordinated Data Analysis Web (NASA, accessed 2025). The Sym-H data are also available from the WDC for Geomagnetism, Kyoto who prepared this index (WDC for Geomagnetism, accessed 2025). The authors thank C Forsyth for making his substorm list available. Even though it was not used for the final version of TiVIE, it greatly helped in the development. The combined data which are used to plot the TiVIE maps are available from Zenodo, (Walach & Grocott, 2024c). Alongside the manuscript, TiVIE light, which generates plots similar to the ones shown in this paper is available to download from Zenodo (Walach & Grocott, 2024a, 2024b).

Acknowledgments

M.-T. W. and A. G. were supported by Natural Environments Research Council (NERC), UK, grant nos. NE/P001556/1, NE/T000937/1, NE/V00283X/1 and NE/V002686/1. M.-T. W. also acknowledges support from the STFC Ernest Rutherford Fellowship programme ST/X003663/1. We acknowledge the use of the High End Computing Facility (HEC) at Lancaster University. Figures 4, 7 and 11 were generated using the Python programming language (v 3.9.13) using a number of packages: matplotlib (Hunter, 2007); numpy (van der Walt et al., 2011); PyDARNio (SuperDARN Data Standards Working Group et al., 2021); AACGM v2 (Burrell et al., 2018) and (Shepherd, 2014). We acknowledge the use of pyDARN (SuperDARN Data Visualization Working Group et al., 2023), which has also greatly benefited from the SuperDARN community's help. We also acknowledge the use of SciPy (Virtanen et al., 2020) and xarray (Hoyer & Hamman, 2017).

References

Baker, J. B. H., Greenwald, R. A., Ruohoniemi, J. M., Forster, M., Paschmann, G., Donovan, E. F., … Balogh, A. (2004, January). Conjugate comparison of Super Dual Auroral Radar Network and Cluster electron drift instrument measurements of E x B plasma drift. *J. Geophys. Res.*, *109*(A1). doi: 10.1029/2003JA009912

Baker, K. B., & Wing, S. (1989, July). A new magnetic coordinate system for conjugate studies at high-latitudes. *J. Geophys. Res.*, *94*(A7), 9139-9143.

British Antarctic Survey. (2017). *British Antarctic Survey SuperDARN Mirror [dataset].* online. Retrieved from `https://www.bas.ac.uk/project/superdarn/#data`

Burrell, A., van der Meeren, C., & Laundal, K. M. (2018). *aburrell/aacgmv2:aacgmv2 2.5.1 (2.5.1).* Zenodo. Retrieved from `https://doi.org/10.5281/zenodo.1469697` doi: 10.5281/zenodo.1469697

Cerisier, J.-C., & Senior, C. (1994). *Merge:a fortran program.* Cent. d'Etude des Environments Terr. et Planet., Cent. Nat. de la Rech. Si.

Chisham, G., Lester, M., Milan, S. E., Freeman, M. P., Bristow, W. A., Grocott, A., … Walker, A. D. M. (2007, January). A decade of the Super Dual Auroral Radar Network (SuperDARN): scientific achievements, new techniques and future directions. *Surveys in Geophysics*, *28*, 33-109. doi: 10.1007/s10712-007-9017-8

Chisham, G., & Pinnock, M. (2002, January). Assessing the contamination of SuperDARN global convection maps by non-F-region backscatter. *Ann. Geophysicae*, *20*(1), 13-28.

Chisham, G., Yeoman, T. K., & Sofko, G. J. (2008). Mapping ionospheric backscatter measured by the superdarn hf radars - part 1: A new empirical virtual height model. *Annales Geophysicae*, *26*(4), 823–841. Retrieved from `https://angeo.copernicus.org/articles/26/823/2008/` doi: 10.5194/angeo-26-823-2008

Cousins, E. D. P., & Shepherd, S. G. (2010). A dynamical model of high-latitude convection derived from SuperDARN plasma drift measurements. *J. Geophys. Res.*, *115*. doi: 10.1029/2010JA016017

Cowley, S. W. H., & Lockwood, M. (1992, February). Excitation and decay of solar wind-driven flows in the magnetosphere-ionosphere system. *Ann. Geophysicae*, *10*, 103-115.

Coxon, J. C., Chisham, G., Freeman, M. P., Forsyth, C., Walach, M.-T., Murphy, K. R., ... Fogg, A. R. (2023). Extreme birkeland currents are more likely during geomagnetic storms on the dayside of the earth. *Journal of Geophysical Research: Space Physics*, *128*(12), e2023JA031946. Retrieved from `https://agupubs.onlinelibrary.wiley.com/doi/abs/10.1029/2023JA031946` (e2023JA031946 2023JA031946) doi: https://doi.org/10.1029/2023JA031946

Forsyth, C., Rae, I. J., Coxon, J. C., Freeman, M. P., Jackman, C. M., Gjerloev, J., & Fazakerley, A. N. (2015). A new technique for determining substorm onsets and phases from indices of the electrojet (sophie). *Journal of Geophysical Research: Space Physics*, *120*(12), 10,592-10,606. Retrieved from `https://agupubs.onlinelibrary.wiley.com/doi/abs/10.1002/2015JA021343` doi: https://doi.org/10.1002/2015JA021343

Frey, H. U., Mende, S. B., Angelopoulos, V., & Donovan, E. F. (2004, October). Substorm onset observations by IMAGE-FUV. *J. Geophys. Res.*, *109*(A18), A10304. doi: 10.1029/2004JA010607

Gillies, D. M., McWilliams, K. A., St Maurice, J.-P., & Milan, S. E. (2011). Global-scale observations of ionospheric convection during geomagnetic storms. *J. Geophys. Res.*, *116*(A12). doi: 10.1029/2011JA017086

Greenwald, R. A., Baker, K. B., Dudeney, J. R., Pinnock, M., Jones, T. B., Thomas, E. C., ... Yamagishi, H. (1995, February). Darn/SuperDarn: A global view of the dynamics of high-latitude convection. *Space Sci. Rev.*, *71*, 761-796. doi: 10.1007/BF00751350

Grocott, A. (2017). Time-dependence of dawn-dusk asymmetries in the terrestrial ionospheric convection pattern. In S. E. Haaland, A. Runov, & C. Forsyth (Eds.), *Dawn-dusk asymmetries in planetary plasma environments* (p. 107-124). Wiley.

Grocott, A., Cowley, S. W. H., & Sigwarth, J. B. (2003, February). Ionospheric flow during extended intervals of northward but B_Y-dominated IMF. *Ann. Geophysicae*, *21*, 509-538.

Grocott, A., Cowley, S. W. H., Sigwarth, J. B., Watermann, J. F., & Yeoman, T. K. (2002, October). Excitation of twin-vortex flow in the nightside high-latitude ionosphere during an isolated substorm. *Ann. Geophysicae*, *20*, 1577-1601.

Grocott, A., Laurens, H. J., & Wild, J. A. (2017). Nightside ionospheric convection asymmetries during the early substorm expansion phase: Relationship to onset local time. *Geophys. Res. Lett..*, *44*. doi: 10.1002/2017GL075763

Grocott, A., Lester, M., Parkinson, M. L., Yeoman, T. K., Dyson, P. L., Devlin, J. C., & Frey, H. U. (2006, December). Towards a synthesis of substorm electrodynamics: HF radar and auroral observations. *Ann. Geophysicae*, *24*, 3365-3381.

Grocott, A., & Milan, S. E. (2014). The influence of IMF clock angle timescales on the morphology of ionospheric convection. *J. Geophys. Res.*, *119*(7), 5861–5876. doi: 10.1002/2014JA020136

Grocott, A., Milan, S. E., Sato, N., Wild, J. A., Yeoman, T. K., & Yukimatu, A. S. (2010). Superposed epoch analysis of the ionospheric convection evolution during substorms: IMF B_Y dependence. *J. Geophys. Res.*, *115*. doi: 10.1029/2010JA015728

Grocott, A., Milan, S. E., & Yeoman, T. K. (2008, April). Interplanetary magnetic field control of fast azimuthal flows in the nightside high-latitude ionosphere. *Geophys. Res. Lett.*, *35*, L08102. doi: 10.1029/2008GL033545

Grocott, A., Wild, J. A., Milan, S. E., & Yeoman, T. K. (2009). Superposed epoch analysis of the ionospheric convection evolution during substorms: onset latitude dependence. *Ann. Geophysicae*, *27*(2), 591-600.

Grocott, A., Yeoman, T. K., Milan, S. E., Amm, O., Frey, H. U., Juusola, L., ... Takada, T. (2007, July). Multi-scale observations of magnetotail flux transport during IMF-northward non-substorm intervals. *Ann. Geophysicae*, *25*, 1709-1720.

Grocott, A., Yeoman, T. K., Milan, S. E., & Cowley, S. W. H. (2005, July). Interhemispheric observations of the ionospheric signature of tail reconnection during IMF-northward non-substorm intervals. *Ann. Geophysicae*, *23*, 1763-1770.

Grocott, A., Yeoman, T. K., Nakamura, R., Cowley, S. W. H., Frey, H. U., Rème, H., & Klecker, B. (2004, April). Multi-instrument observations of the ionospheric counterpart of a bursty bulk flow in the near-Earth plasma sheet. *Ann. Geophysicae*, *22*, 1061-1075.

Heppner, J. P., & Maynard, N. C. (1987, May). Empirical high-latitude electric-field models. *J. Geophys. Res.*, *92*(A5), 4467-4489.

Hoyer, S., & Hamman, J. (2017). xarray: N-D labeled arrays and datasets in Python. *Journal of Open Research Software*, *5*(1). Retrieved from `https://doi.org/10.5334/jors.148` doi: 10.5334/jors.148

Huang, Y., Richmond, A. D., Deng, Y., & Roble, R. (2012). Height distribution of joule heating and its influence on the thermosphere. *Journal of Geophysical Research: Space Physics*, *117*(A8). Retrieved from `https://agupubs.onlinelibrary.wiley.com/doi/abs/10.1029/2012JA017885` doi: 10.1029/2012JA017885

Hunter, J. D. (2007). Matplotlib: A 2d graphics environment. *Computing in Science & Engineering*, *9*(3), 90–95. doi: 10.1109/MCSE.2007.55

Imber, S. M., Milan, S. E., & Lester, M. (2013). The Heppner-Maynard Boundary measured by SuperDARN as a proxy for the latitude of the auroral oval. *J. Geophys. Res.*, *118*(2), 685-697. doi: 10.1029/2012JA018222

Lewis, R. V., Freeman, M. P., Rodger, A. S., Reeves, G. D., & Milling, D. K. (1997). The electric field response to the growth phase and expansion phase onset of a small isolated substorm. *Annales Geophysicae*, *15*(3), 289–299. Retrieved from `https://doi.org/10.1007/s00585-997-0289-6` doi: 10.1007/s00585-997-0289-6

Liu, H.-L., Bardeen, C. G., Foster, B. T., Lauritzen, P., Liu, J., Lu, G., ... Wang, W. (2018). Development and validation of the whole atmosphere community climate model with thermosphere and ionosphere extension (waccm-x 2.0). *Journal of Advances in Modeling Earth Systems*, *10*(2), 381-402. Retrieved from `https://agupubs.onlinelibrary.wiley.com/doi/abs/10.1002/2017MS001232` doi: 10.1002/2017MS001232

Milan, S. E., Hubert, B., & Grocott, A. (2005, January). Formation and motion of a transpolar arc in response to dayside and nightside reconnection. *J. Geophys. Res.*, *110*(A9), A01212. doi: 10.1029/2004JA010835

Morelli, J. P., Bunting, R. J., Cowley, S. W. H., Farrugia, C. J., Freeman, M. P., Friis-Christensen, E., ... Yeoman, T. K. (1995, November). Radar observations of auroral zone flows during a multiple-onset substorm. *Ann. Geophysicae*, *13*, 1144-1163.

Nagai, T., Fujimoto, M., Saito, Y., Machida, S., Terasawa, T., Nakamura, R., ... Kokubun, S. (1998). Structure and dynamics of magnetic reconnection for substorm onsets with geotail observations. *Journal of Geophysical Research: Space Physics*, *103*(A3), 4419-4440. Retrieved from `https://agupubs.onlinelibrary.wiley.com/doi/abs/10.1029/97JA02190` doi: 10.1029/97JA02190

NASA. (accessed 2025). *SPDF Coordinated Data Analysis Web [dataset].* online. Retrieved from `https://cdaweb.gsfc.nasa.gov/index.html/`

Newell, P. T., & Gjerloev, J. W. (2011). Evaluation of supermag auroral electrojet indices as indicators of substorms and auroral power. *Journal of Geophysical Research: Space Physics*, *116*(A12). Retrieved from `https://agupubs.onlinelibrary.wiley.com/doi/abs/10.1029/2011JA016779` doi: 10.1029/2011JA016779

Ohtani, S., & Gjerloev, J. W. (2020). Is the substorm current wedge an ensemble of wedgelets?: Revisit to midlatitude positive bays. *Journal of Geophysical Research: Space Physics*, *125*(9), e2020JA027902. Retrieved from `https://agupubs.onlinelibrary.wiley.com/doi/abs/10.1029/2020JA027902` (e2020JA027902 2020JA027902) doi: https://doi.org/10.1029/2020JA027902

Orr, L., Grocott, A., Walach, M.-T., Chisham, G., Freeman, M. P., Lam, M. M., & Shore, R. M. (2023). A quantitative comparison of high latitude electric field models during a large geomagnetic storm. *Space Weather*, *21*(1), e2022SW003301. Retrieved from `https://agupubs.onlinelibrary.wiley.com/doi/abs/10.1029/2022SW003301` (e2022SW003301 2022SW003301) doi: https://doi.org/10.1029/2022SW003301

Pettigrew, E. D., Shepherd, S. G., & Ruohoniemi, J. M. (2010). Climatological patterns of high-latitude convection in the northern and southern hemispheres: Dipole tilt dependencies and interhemispheric comparisons. *J. Geophys. Res.*, *115*. doi: 10.1029/2009JA014956

Provan, G., Lester, M., Mende, S., & Milan, S. (2004, October). Statistical study of high-latitude plasma flow during magnetospheric substorms. *Ann. Geophysicae*, *22*, 3607-3624.

Ruohoniemi, J. M., & Baker, K. B. (1998, September). Large-scale imaging of high-latitude convection with Super Dual Auroral Radar Network HF radar observations. *J. Geophys. Res.*, *103*, 20797-20811. doi: 10.1029/98JA01288

Ruohoniemi, J. M., & Greenwald, R. A. (1996, October). Statistical patterns of high-latitude convection obtained from Goose Bay HF radar observations. *J. Geophys. Res.*, *101*, 21743-21764. doi: 10.1029/96JA01584

Ruohoniemi, J. M., & Greenwald, R. A. (2005, September). Dependencies of high-latitude plasma convection: Consideration of interplanetary magnetic field, seasonal, and universal time factors in statistical patterns. *J. Geophys. Res.*, *110*(A9). doi: 10.1029/2004JA010815

Shepherd, S., & Ruohoniemi, J. (2000, October). Electrostatic potential patterns in the high-latitude ionosphere constrained by SuperDARN measurements. *J. Geophys. Res.*, *105*(A10), 23005-23014.

Shepherd, S. G. (2014). Altitude-adjusted corrected geomagnetic coordinates: Definition and functional approximations. *Journal of Geophysical Research: Space Physics*, *119*(9), 7501-7521. Retrieved from `https://agupubs.onlinelibrary.wiley.com/doi/abs/10.1002/2014JA020264` doi: 10.1002/2014JA020264

SuperDARN Data Standards Working Group, Krieger, K. J., Kotyk, K., Detwiller, M. H., Billett, D. D., Burrell, A. G., … Schmidt, M. T. (2021). *Superdarn/pydarnio: pydarnio v1.1 (v1.1).* Zenodo. Retrieved from `https://doi.org/10.5281/zenodo.4792463` doi: 10.5281/zenodo.4792463

SuperDARN Data Visualization Working Group, Martin, C. J., Shi, X., Schmidt, M. T., Day, E. K., Bland, E. C., … Krieger, K. J. (2023). *Superdarn/pydarn: pydarn v3.1.1 (v3.1.1).* Zenodo. Retrieved from `https://doi.org/10.5281/zenodo.7767590` doi: 10.5281/zenodo.7767590

SuperDARN Data Analysis Working Group, P. m., Thomas, E. G., Ponomarenko, P. V., Billett, D. D., Bland, E. C., Burrell, A. G., … Walach, M.-T. (2018, August). *Superdarn radar software toolkit (rst) 4.2.* Retrieved from `https://doi.org/10.5281/zenodo.1403226` doi: 10.5281/zenodo.1403226

Thomas, E. G., & Shepherd, S. G. (2018, April). Statistical Patterns of Ionospheric Convection Derived From Mid-latitude, High-Latitude, and Polar SuperDARN

HF Radar Observations. *J. Geophys. Res-Space Phys.*, *123*(4), 3196–3216. doi: 10.1002/2018JA025280

van der Walt, S., Colbert, S. C., & Varoquaux, G. (2011). The numpy array: A structure for efficient numerical computation. *Computing in Science & Engineering*, *13*(2), 22-30. doi: 10.1109/MCSE.2011.37

Virtanen, P., Gommers, R., Oliphant, T. E., Haberland, M., Reddy, T., Cournapeau, D., ... SciPy 1.0 Contributors (2020). SciPy 1.0: Fundamental Algorithms for Scientific Computing in Python. *Nature Methods*, *17*, 261–272. doi: 10.1038/s41592-019-0686-2

Walach, M.-T., & Grocott, A. (2019). Superdarn observations during geomagnetic storms, geomagnetically active times, and enhanced solar wind driving. *Journal of Geophysical Research: Space Physics*, *124*(7), 5828-5847. Retrieved from https://agupubs.onlinelibrary.wiley.com/doi/abs/10.1029/2019JA026816 doi: 10.1029/2019JA026816

Walach, M.-T., & Grocott, A. (2024a, August). *mtwalach/tivie_light: v1.0.* Zenodo. Retrieved from https://doi.org/10.5281/zenodo.13271264 doi: 10.5281/zenodo.13271264

Walach, M.-T., & Grocott, A. (2024b, August). *Time Variable Ionospheric Electric Field Model (TiVIE) light data v 1.0 [dataset].* Zenodo. Retrieved from https://doi.org/10.5281/zenodo.13271014 doi: 10.5281/zenodo.13271014

Walach, M.-T., & Grocott, A. (2024c, August). *The Time Variable Ionospheric Electric Field (TiVIE) Model Outputs v 1.0 [dataset].* Zenodo. Retrieved from https://doi.org/10.5281/zenodo.13270754 doi: 10.5281/zenodo.13270754

Walach, M.-T., Grocott, A., & Milan, S. E. (2021). Average ionospheric electric field morphologies during geomagnetic storm phases. *Journal of Geophysical Research: Space Physics*, *126*(4), e2020JA028512. Retrieved from https://agupubs.onlinelibrary.wiley.com/doi/abs/10.1029/2020JA028512 (e2020JA028512 2020JA028512) doi: https://doi.org/10.1029/2020JA028512

Walach, M.-T., Grocott, A., Staples, F., & Thomas, E. G. (2022). Super dual auroral radar network expansion and its influence on the derived ionospheric convection pattern. *Journal of Geophysical Research: Space Physics*. doi: https://doi.org/10.1029/2021JA029559

Walach, M.-T., Grocott, A., Thomas, E. G., & Staples, F. (2022). Dusk-dawn asymmetries in superdarn convection maps. *Journal of Geophysical Research: Space Physics*, *127*(12), e2022JA030906. Retrieved from https://agupubs.onlinelibrary.wiley.com/doi/abs/10.1029/2022JA030906 doi: https://doi.org/10.1029/2022JA030906

Walach, M.-T., & Milan, S. E. (2015). Are steady magnetospheric convection events prolonged substorms? *J. Geophys. Res.*, *120*(3), 1751–1758. doi: 10.1002/2014JA020631

Walach, M.-T., Milan, S. E., Murphy, K. R., Carter, J. A., Hubert, B. A., & Grocott, A. (2017). Comparative study of large-scale auroral signatures of substorms, steady magnetospheric convection events, and sawtooth events. *Journal of Geophysical Research: Space Physics*, *122*(6), 6357-6373. Retrieved from https://agupubs.onlinelibrary.wiley.com/doi/abs/10.1002/2017JA023991 doi: 10.1002/2017JA023991

WDC for Geomagnetism. (accessed 2025). *Sym-H index [dataset].* online. Retrieved from http://wdc.kugi.kyoto-u.ac.jp/wdc/Sec3.html

Weimer, D. R. (2001, January). An improved model of ionospheric electric potentials including substorm perturbations and application to the Geospace Environment Modeling November 24, 1996, event. *J. Geophys. Res-Space Phys.*, *106*(A1), 407–416.

Yeoman, T. K., Davies, J. A., Wade, N. M., Provan, G., & Milan, S. E. (2000, September). Combined CUTLASS, EISCAT and ESR observations of ionospheric plasma flows at the onset of an isolated substorm. *Ann. Geophysicae*, *18*, 1073-1087.